# A High-Fidelity Benthic Stable Isotope Record of Late Cretaceous-Early Eocene Climate Change and Carbon-Cycling

Barnet James, Stewart Kinmond (Orcid ID: 0000-0003-3885-5664)
Westerhold Thomas (Orcid ID: 0000-0001-8151-4684)
Leng Melanie J., J (Orcid ID: 0000-0003-1115-5166)
Bailey Ian (Orcid ID: 0000-0001-5150-5437)
Röhl Ursula (Orcid ID: 0000-0001-9469-7053)
Zachos James, C (Orcid ID: 0000-0001-8439-1886)

# A High-Fidelity Benthic Stable Isotope Record of Late Cretaceous–Early Eocene Climate Change and Carbon-Cycling

**J. S. K. Barnet[1*], K. Littler[1], T. Westerhold[2], Dick Kroon[3], M. J. Leng[4], I. Bailey[1], U. Röhl[2], and J. C. Zachos[5]**

[1] Camborne School of Mines & Environment and Sustainability Institute, University of Exeter, Penryn Campus, Cornwall, TR10 9FE, UK.

[2] MARUM – Center for Marine Environmental Sciences, University of Bremen, Leobener Strasse 8, 28359, Bremen, Germany.

[3] School of GeoSciences, University of Edinburgh, Edinburgh, EH9 3JW, UK.

[4] NERC Isotope Geosciences Facility, British Geological Survey, Nottingham, NG12 5GG, UK and Centre for Environmental Geochemistry, School of Biosciences, Sutton Bonington Campus, University of Nottingham, Loughborough, LE12 5RD, UK.

[5] Department of Earth and Planetary Sciences, University of California Santa Cruz, 1156 High Street, Santa Cruz, California, 95064, USA

*Corresponding author: James Barnet (jb688@exeter.ac.uk)

**Key Points:**

- 405-kyr and 100-kyr eccentricity forced the climate and carbon cycle, with carbon cycle perturbations lagging climate during this time
- Elevated global temperatures and atmospheric $pCO_2$ during LIP volcanism increased climate and carbon cycle sensitivity to orbital forcing
- The frequency of hyperthermals suggests that carbon was periodically released from a dynamic reservoir which could be replenished quickly

This article has been accepted for publication and undergone full peer review but has not been through the copyediting, typesetting, pagination and proofreading process which may lead to differences between this version and the Version of Record. Please cite this article as doi: 10.1029/2019PA003556

**Abstract**

The Late Cretaceous–Early Paleogene is the most recent period in Earth history that experienced sustained global greenhouse warmth on multi-million year timescales. Yet, knowledge of ambient climate conditions and the complex interplay between various forcing mechanisms are still poorly constrained. Here we present a 14.75 million year-long, high-resolution, orbitally-tuned record of paired climate change and carbon-cycling for this enigmatic period (~67–52 Ma), which we compare to an up-to-date compilation of atmospheric $pCO_2$ records. Our climate and carbon-cycling records, which are the highest resolution stratigraphically complete records to be constructed from a single marine site in the Atlantic Ocean, feature all major transient warming events (termed "hyperthermals") known from this time period. We identify eccentricity as the dominant pacemaker of climate and the carbon cycle throughout the Late Maastrichtian to Early Eocene, through the modulation of precession. On average, changes in the carbon cycle lagged changes in climate by ~23,000 years at the long eccentricity (405,000 year) band, and by ~3,000–4,500 years at the short eccentricity (100,000 year) band, suggesting that light carbon was released as a positive feedback to warming induced by orbital forcing. Our new record places all known hyperthermals of the Late Maastrichtian–Early Eocene into temporal context with regards to evolving ambient climate of the time. We constrain potential carbon cycle influences of Large Igneous Province volcanism associated with the Deccan Traps and North Atlantic Igneous Province, as well as the sensitivity of climate and the carbon-cycle to the 2.4 million-year-long eccentricity cycle.

**Plain language summary**

The study of globally warm climates and short-lived warming events in Earth's past can provide unrivaled insights into the challenges that mankind may face over the next few generations. Using samples recovered from an ocean drill core in the deep South Atlantic, we have generated continuous temperature and carbon cycle records from the calcite shells of a single microfossil species, spanning a period of globally warm climate from 67 to 52 million years ago, before the development of permanent large-scale polar ice sheets. Our record contains a number of rapid warming events, allowing us to determine their origin. We find that changes in the shape of Earth's orbit around the Sun initiated warming at Earth's surface, which was then amplified by the release of greenhouse gases from temperature- or climate-sensitive carbon stores (e.g., peat, permafrost or methane hydrates). These rapid warming events increased in frequency and magnitude during the warmer climate intervals characterized by significant volcanic activity, suggesting that such carbon stores become more unstable during warmer climates. As our climate warms at unprecedented rates, the release of greenhouse gases from naturally-occurring temperature- or climate-sensitive carbon stores could also form an additional and largely unconstrained contribution to future climate change.

## 1 Introduction

The global greenhouse climate of the latest Cretaceous to Early Paleogene (~67–52 million years ago, Ma) has been the subject of heightened interest in recent years, largely because this interval was punctuated by massive upheavals in both the geosphere and biosphere, including a bolide impact at the Cretaceous/Paleogene (K/Pg) boundary (66.02 Ma; Schulte et al., 2010), LIP volcanism in the Deccan Traps (~66 Ma; Renne et al., 2015; Schoene et al., 2015), and North Atlantic Igneous Province (NAIP; ~63–60 & ~57.5–54 Ma; Sinton & Duncan, 1998), and transient "hyperthermals", such as the Paleocene–Eocene Thermal Maximum (PETM, ~55.9 Ma; McInerney & Wing, 2011). The release of massive quantities of greenhouse gases (either carbon dioxide or methane) over a geologically brief time period of 10's of thousands of years, rapid global warming at both Earth's surface and in the deep-ocean, and acidification of the oceans resulting in enhanced dissolution of deep-sea carbonates, characterized many of these hyperthermal events (McInerney & Wing, 2011; Zachos et al., 2005). Many proxy and modeling studies have focused on the hyperthermal events (e.g., Panchuk et al., 2008; Zeebe et al., 2009), since they may represent the closest geological analogues for future anthropogenic climate change, but our knowledge of background ambient climate outside of these events is incomplete.

Orbital cyclicity of varying frequencies acts as the pacemaker of Earth's climate system and carbon cycle throughout the Cretaceous and Paleogene (e.g., Husson et al., 2011; Kirtland Turner et al., 2014; Sexton et al., 2011), with the well-studied Late Paleocene–Early Eocene hyperthermals known to be paced by the 100,000 and 405,000 year (100- and 405-kyr) eccentricity beat (Littler et al., 2014; Westerhold et al., 2017; Zachos et al., 2010). While Eocene hyperthermals such as the PETM have been studied extensively with geochemical, paleontological, sedimentological and modeling techniques, much of the climate of the preceding Paleocene has been comparatively neglected, with only lower resolution semi-continuous single-site records and stacked records from multiple sites spanning this time interval (Cramer et al., 2009; Westerhold et al., 2011, 2018; Zachos et al., 2001, 2008). Indeed, a number of smaller climatic perturbations have recently been proposed in the latest Maastrichtian (Late Maastrichtian warming event; LMWE; ~66.2 Ma; Barnet et al., 2017) and the Early–Middle Paleocene, including the Dan-C2 event (65.9–65.7 Ma; Quillévéré et al., 2008), the Latest Danian Event (LDE, ~62.1–62.0 Ma; Bornemann et al., 2009; Deprez et al., 2017; Westerhold et al., 2011), and the Danian/Selandian Transition Event (D/STE, ~61.4–61.2 Ma; Arenillas et al., 2008). There is currently little evidence for a deep-sea temperature response for some of these events, such as the Dan-C2, as they have mainly been described from marine continental shelf settings. Establishing whether these and other events are global in scale, and placing them in the context of background orbital scale variability, is essential for ultimately understanding their origin and/or impacts. Moreover, with high-fidelity records of the climate and carbon cycle extending over tens of millions of years, an opportunity exists to assess if and how Earth system sensitivity to cyclical forcing in insolation changes with baseline boundary conditions (e.g., continental geography, ocean gateways and atmospheric greenhouse gas levels).

We present the longest (14.75 million year), highest resolution (1.5–4 kyr), stratigraphically continuous, single-species benthic foraminiferal carbon ($\delta^{13}C_{benthic}$) and oxygen ($\delta^{18}O_{benthic}$) isotope records for the Late Maastrichtian to Early Eocene (~67.1–52.35 Ma) from a single site in the South Atlantic Ocean (Ocean Drilling Program [ODP] Site 1262), calibrated to an updated orbitally-tuned age model. This record, generated by multiple studies, allows us to examine the evolution of climate and carbon-cycling during this enigmatic greenhouse world at unprecedented resolution. Spectral analysis of these records allows us to identify the principle forcing mechanisms, whilst phasing between the records

offers an insight into the genesis of cyclic perturbations to Earth's climate and carbon cycle during this time. We further place all known hyperthermals into a robust cyclostratigraphic framework, and use our record to determine if the poorly studied Early Paleocene Dan-C2 event can be classified as a global hyperthermal, with a pronounced deep-sea temperature response.

## 2 Materials and Methods

### 2.1 Stable isotope record

This study is based on a stratigraphically continuous section of Late Maastrichtian–Early Eocene clayey nannofossil ooze recovered from ODP Site 1262 on Walvis Ridge in the South Atlantic (27°11.15′S, 1°34.62′E; water depth 4759 m, paleo-water depth ~3000–3500 m; Figure 1; Shipboard Scientific Party, 2004). We generated 873 new paired single-species (*Nuttallides truempyi*) $\delta^{13}C_{benthic}$ and $\delta^{18}O_{benthic}$ data for the Early–Middle Paleocene on an IsoPrime 100 Gas Source Isotope Ratio Mass Spectrometer in dual inlet mode equipped with a Multiprep Device, at the Natural Environment Research Council (NERC) Isotope Geosciences Facility, British Geological Survey. Long-term analytical error (1σ) was 0.03 ‰ for $\delta^{13}C$ and 0.05 ‰ for $\delta^{18}O$. We combined our new record with the Late Maastrichtian–Early Danian (Barnet et al., 2017), Late Paleocene–Early Eocene (Littler et al., 2014), PETM (McCarren et al., 2008), Eocene Thermal Maximum 2 (Stap et al., 2010) and Early Eocene (Lauretano et al., 2015) records generated from the same site, to create continuous 14.75 million year-long benthic stable isotope records spanning the Late Maastrichtian to Early Eocene (~67.10–52.35 Ma; Figure 2). Spectral analysis methods are described in Supporting Information Text S5.

### 2.2 Age model

An updated orbitally-tuned age model is provided for this site based on recognition and counting of the stable 405-kyr eccentricity cycle in our $\delta^{13}C_{benthic}$ dataset (Dinarès-Turell et al., 2014; Littler et al., 2014; Westerhold et al., 2008), correlated to the La2010b solution of Laskar et al. (2011) and anchored to astronomical ages of 66.0225 Ma and 55.93 Ma for the K/Pg boundary and PETM, respectively (Dinarès-Turell et al., 2014; Westerhold et al., 2007). Whilst other orbital solutions are available, Westerhold et al. (2017) have recently shown that La2010b represents the optimal astronomical solution for orbital tuning of deep-sea sediment cores older than 52 Ma, based on the modulation of short (100-kyr) eccentricity cycles by long (405-kyr) eccentricity, evident in high-resolution Fe intensity records from multiple Walvis Ridge sites. Age model tie points are provided in Table S3.

### 2.3 Integration of other proxy data

We use the difference between published bulk carbonate carbon isotope ($\delta^{13}C_{bulk}$; Kroon et al., 2007; Littler et al., 2014; Lourens et al., 2005; Zachos et al., 2005, 2010) and our benthic $\delta^{13}C$ data ($\delta^{13}C_{bulk}$–$\delta^{13}C_{benthic}$ gradient) to qualitatively approximate the surface-to-deep carbon isotope gradient and hence relative shifts in surface-ocean dissolved inorganic carbon (DIC) $\delta^{13}C$. We consider this to be a reasonable approach since the majority of the carbonate component of sediments from this site ($\delta^{13}C_{bulk}$) is composed of calcareous nannofossils and planktic foraminifera (Shipboard Scientific Party, 2004). Hence, we recognize that bulk carbonate $\delta^{13}C$ can be influenced by other factors such as changes in assemblages and preservation. Furthermore, we use published elemental Fe intensities as a proxy for terrigenous clay content and therefore for carbonate dissolution (Westerhold et al.,

2007, 2008). We have also produced an up-to-date compilation of over 100 atmospheric $pCO_2$ estimates from 18 different studies, placed onto a common age model. We have recalibrated the $pCO_2$ estimates based on the pedogenic carbonate proxy using the Cerling paleobarometer (Cerling, 1999), with an updated soil-respired $CO_2$ concentration of 2500 ppm (Breecker et al., 2010; see Supporting Information), and have recalibrated those based on the stomatal index proxy after Barclay & Wing (2011), using a power curve regression method.

## 3 Results and discussion

### 3.1 Late Maastrichtian–Early Eocene carbon cycle and climate evolution

We observe an overall long-term decrease in $\delta^{18}O_{benthic}$ values from +0.6 ‰ to –0.7 ‰, corresponding to warming of ~6.5°C, from the Late Maastrichtian (~67.1 Ma) to Early Eocene (~52.3 Ma; Figure 2f). This is accompanied by an overall decrease of ~1.4 ‰ in $\delta^{13}C_{benthic}$ values (Figure 2d), consistent with release of isotopically light carbon into the exogenic carbon cycle, and/or a shift in the relative fluxes of carbon between reservoirs (Komar et al., 2013). This long term decrease in $\delta^{13}C_{benthic}$ values is interrupted by a prominent high in the Late Paleocene corresponding to the well-known Paleocene Carbon Isotope Maximum (PCIM), which likely reflects sequestration of light carbon in reduced marine or terrestrial reservoirs. Although there is considerable scatter and a paucity of Paleocene data, atmospheric $pCO_2$ values generally rise from ~100–700 ppm during the earliest Paleocene to ~100 to >1000 ppm during the Late Paleocene–Early Eocene (Figure 2a), suggesting an overall increase in greenhouse gas levels during this time. Elemental Fe concentrations in sediments deposited at ODP Site 1262 also decreased markedly from the Early Paleocene through to the Early Eocene (Figure 2g), whilst sedimentation rates markedly increase (from ~0.2 to ~1.7 cm/kyr) over the same time interval (Figure 2h). This pattern could be interpreted to reflect increased $CaCO_3$ preservation at the study site as a result of a progressively deepening lysocline, and a corresponding dilution of the terrestrially-derived Fe content. Assuming the calcite compensation depth (CCD) exhibits a similar trend, this pattern would be consistent with proxy data from the Indian Ocean (Slotnick et al., 2015), and modeling studies of the Atlantic and Pacific (Komar et al., 2013). As a result of the general rise in background atmospheric $pCO_2$, lysocline deepening is likely related to a rise in alkalinity due to increased chemical weathering and delivery of solutes to the global ocean under increasingly warm and humid greenhouse conditions during the Late Paleocene to Early Eocene (Hilting et al., 2008). However, some of the Paleocene–Early Eocene elemental Fe intensity and sedimentation rate patterns could be explained by shifts in biogenic carbonate productivity and/or variations in the flux of wind-blown aeolian dust from the African continent, without invoking dissolution of calcium carbonate. This is particularly true for the first 1–2 million years of the Paleocene, when biogenic carbonate productivity was likely to have been significantly reduced following the K/Pg mass extinction (Zachos & Arthur, 1986), resulting in the highest elemental Fe intensities and lowest sedimentation rates (~0.2–0.5 cm/kyr) of the early Paleogene at ODP Site 1262 (Figure 2g,h).

Superimposed on Late Maastrichtian to Early Eocene warming were shorter-term shifts in Earth's climate and biosphere. At ODP Site 1262, the mass extinction within marine biota across the K/Pg boundary is accompanied by a highly unusual reversal of the surface-to-deep carbon isotope gradient ($\delta^{13}C_{bulk}$ shifts by > –2.5 ‰ whereas $\delta^{13}C_{benthic}$ changes by only ~–0.8 ‰; Figure 2c,d,e). This apparent reversal can be explained by extreme vital effects within the very small opportunistic planktic foraminifera species which evolved in the immediate aftermath of the K/Pg boundary (Birch et al., 2012, 2013), along with partial collapse of the biological pump following the K/Pg mass extinction (D'Hondt et al., 1998),

resulting in reduced surface water primary productivity and decreased remineralization of isotopically more negative $C_{org}$ at depth (Birch et al., 2016). The pre-K/Pg surface-to-deep isotope gradient was not completely restored until the Danian/Selandian Transition Event (D/STE), over 4.5 million years after the K/Pg mass extinction, suggesting long-term disruption to marine ecosystems and the carbon cycle (Figure 2e).

The coolest conditions of the Paleocene occurred between ~61–58 Ma, broadly coincident with the PCIM, when our study site was characterized by bottom water temperatures of ~7°C (Figure 2f). Cooler global temperatures at this time were likely facilitated by the burial of significant volumes of carbon in either biogenic $CH_4$ hydrates beneath the continental shelves (Dickens, 2003), low-latitude peat deposits (Kurtz et al., 2003), or high-latitude permafrost (DeConto et al., 2012), to produce the positive carbon isotope signature of the ocean-atmosphere system that we observe. This period of cool temperatures and carbon sequestration was followed by a long-term warming trend from the Late Paleocene–Early Eocene, triggered by rising atmospheric $pCO_2$ levels and perhaps an intensification of bottom water mass exchange between the North and South Atlantic, enhancing poleward heat transport (Batenburg et al., 2018). Significant temperature- and climate-sensitive carbon reservoirs were therefore primed to be episodically released as ambient climate warmed and periodically crossed critical thresholds, resulting in pulsed release during the hyperthermals and smaller climatic perturbations of the Late Paleocene to Early Eocene (Zachos et al., 2010).

### 3.2 Comparison between the South Atlantic and equatorial Pacific

A comparison between the new benthic stable isotope records from ODP Site 1262 and published coeval records from equatorial Pacific ODP Site 1209 (Westerhold et al., 2011, 2018), highlights the synchronicity of the long-term trends exhibited by the deep-sea carbon isotopes and temperature between both ocean basins, demonstrating the trends are indeed global (Figure 3). Similarly, many of the hyperthermal events and smaller climatic perturbations identified within our records from ODP Site 1262 are also expressed within the equatorial Pacific record. Moreover, the ODP Site 1209 $\delta^{13}C_{benthic}$ data are generally offset from the ODP Site 1262 data towards more negative values, typically by ~–0.2–0.4 ‰, suggestive of an older deep-water mass (characterized by a lighter carbon isotope signature) bathing the equatorial Pacific site (Figure 3). This is broadly consistent with independent evidence for early Paleogene ocean circulation patterns inferred from neodymium isotope data, which suggest a bi-modal source of deep-water formation from North Pacific Deep Water (NPDW) and South Pacific Deep Water (SPDW) sources in the Pacific, but a single source from the Southern Ocean in the Atlantic (Batenburg et al., 2018; Thomas, D.J. et al., 2003, 2008; Figure 1). Based on the paleo-latitudes of ODP Site 1262 and ODP Site 1209 during the early Paleogene (Figure 1), ODP Site 1262 would have been located significantly closer to deep-water formation in the Atlantic sector of the Southern Ocean than ODP Site 1209 would have been to the source regions of either SPDW or NPDW (Figure 1).

The Atlantic-Pacific offset in $\delta^{13}C_{benthic}$ is not stable throughout the latest Cretaceous to Early Eocene, suggesting periodic decoupling between the two basins. Periods characterized by decoupling between the Atlantic and Pacific include the collapse of the gradient in the aftermath of the K/Pg boundary, apparently antiphase behavior during the latest Maastrichtian, and a reduction in the gradient following the PETM (Figure 3). The collapse in surface-ocean primary productivity following the K/Pg mass extinction is likely to be the primary explanation for the reduction in the Atlantic-Pacific gradient at the start of the Paleocene, which would have resulted in less negative $\delta^{13}C_{benthic}$ values in the oldest deep-ocean water masses globally. There is also evidence, however, for transient shifts in the predominance of NPDW and SPDW sources in the equatorial Pacific during the Late

Maastrichtian based on neodymium isotopes (Dameron et al., 2017). These include an influx of older and more corrosive SPDW during the LMWE, and a reversal to younger less corrosive predominantly NPDW as the climate cooled during the LMWE recovery. Assuming there are no age model inconsistencies between the Atlantic and Pacific sites, the incursion of an older water mass during the LMWE may explain the antiphase behavior between the carbon isotope records across this event. Meanwhile, the incursion of younger NPDW immediately prior to the K/Pg boundary may also account for a portion of the collapse in the carbon isotope gradient immediately before and following the K/Pg boundary, as the relative difference in the age of the water masses bathing ODP Sites 1262 and 1209 during this time may have been reduced. Although the development of a low latitude source(s) of salty deep water proximal to the Pacific may have contributed to the reduction in the carbon isotope gradient between the Atlantic and Pacific during and following the PETM (Bice et al., 1997), a reduction in the volume of deep-water production in the Southern Ocean may have occurred due to polar amplification of surface-ocean warming in the high latitudes (Lunt et al., 2010). A change to a more slugglish thermohaline circulation during this time may have decreased ventilation of deep-ocean bottom waters, explaining evidence for benthic foraminiferal extinction (Thomas, E., 2003), as well as partially homogenized differences in age of the deep water masses between the Atlantic and Pacific.

### 3.3 Was the Dan-C2 event a global hyperthermal?

Our high-resolution records also shed new light on the Dan-C2 event of the Early Paleocene and whether this event can be classified as a small global hyperthermal, analogous to others of the Early Paleocene such as the LDE (Figure 4; Figure 5; see Figure 2 for stratigraphic positions of the Dan-C2 and LDE). The Dan-C2 event is characterized by significant negative excursions within planktic foraminiferal and bulk carbonate carbon and oxygen isotope data from the South Atlantic (Kroon et al., 2007), NW Atlantic (Quillévéré et al., 2008) and Tethyan margin (Coccioni et al., 2010; Figure 4b), and also appears to be orbitally-paced, with inception during the first 405-kyr eccentricity maximum ($Pc_{405}1$) of the Paleocene, following the K/Pg boundary (Figure 4a). This led some to suggest that the Dan-C2 event could represent the first hyperthermal of the Paleocene epoch (Quillévéré et al., 2008; Coccioni et al., 2010), even though no existing benthic records exhibit a strong temperature response. We observe no transient bottom water warming in our new high-resolution $\delta^{18}O_{benthic}$ data from ODP Site 1262 during this supposed event, in agreement with lower resolution $\delta^{18}O_{benthic}$ data from the equatorial Pacific and NW Atlantic (Quillévéré et al., 2008; Westerhold et al., 2011), strongly suggesting that the global deep ocean did not warm during Dan-C2 (Figure 4c; Figure 5b). Similarly, in contrast to the large negative excursion observed in $\delta^{13}C_{bulk}$ (Kroon et al., 2007; Figure 4b), we also observe a muted response during the event in our $\delta^{13}C_{benthic}$ data from ODP Site 1262 (Figure 4c; Figure 5a). The significantly larger excursion in $\delta^{13}C_{bulk}$ (Figure 4b), which is dominated by signals from calcareous nannofossils and planktic foraminifera, is likely an artefact due to a combination of: a) a significant reduction in surface-ocean productivity, and b) the proliferation of unusually small opportunistic planktic foraminifera species characterized by extreme vital effects immediately prior to the onset of Dan-C2 (Birch et al., 2012, 2013). Whilst the time interval immediately following the K/Pg mass extinction is characterized by the highest Fe intensities and lowest sedimentation rates at ODP Site 1262 (Figure 2g,h; Figure 4d; Figure 5c), the lack of a significant change in preservation of benthic foraminifera during this event (Figure S1) suggests that these geochemical and sedimentological characteristics are the result of a significant reduction in biogenic carbonate productivity within the surface ocean (hence reduced dilution of Fe-rich terrigenous clay), rather than severe dissolution of calcium carbonate during Dan-C2 (Zachos & Arthur, 1986). Conversely, Westerhold et al. (2011)

describe a marked increase in sedimentation rates during the first 700 kyr of the Paleocene at ODP Site 1209 (i.e., a drop in Fe intensity and a spike in % coarse fraction), which may reflect a rise in carbonate saturation state and increased preservation of calcium carbonate in the deep ocean during this time. A global deepening of the CCD is believed to have occurred in the aftermath of the K/Pg mass extinction, following a reduction in surface ocean carbonate production (Zachos et al., 1989). Combined with the lack of evidence for deep-sea warming, we suggest that Dan-C2 cannot be classified as a typical global hyperthermal, analogous to the LDE (Figure 5). We propose that the Dan-C2 event could reflect a relatively small carbon cycle and climatic response to the first 405-kyr eccentricity maximum of the Paleocene, with a magnified expression within bulk carbonate and planktic carbon isotope records (Figure 4b), along with dissolution proxy records (Figure 4d), due to the peculiar oceanographic conditions (i.e., partial collapse of the biological pump and extreme vital effects within opportunistic planktic foraminifera taxa) following the K/Pg mass extinction (Birch et al., 2012, 2013, 2016; D'Hondt et al., 1998; Zachos & Arthur, 1986). Alternatively, the Dan-C2 could represent a climate and carbon cycle perturbation of regional but not global significance, with an expression confined to the surface ocean of the mid-latitude Atlantic and Tethys, but not affecting the high-latitude regions of deep-water formation (i.e., Southern Ocean and North Pacific). Furthermore, ongoing Deccan volcanism may have contributed to generally elevated atmospheric $pCO_2$ levels and global temperatures during this time (Renne et al., 2015; Schoene et al., 2015; Figure 2i), potentially increasing the sensitivity of the climate and carbon cycle to the first 405-kyr eccentricity maximum of the Paleocene.

### 3.4 Spectral analysis

#### 3.4.1 Orbital pacing of Late Maastrichtian–Early Eocene changes in climate and the carbon cycle

Similar to the findings of other studies of the early Paleogene (Husson et al., 2011; Kirtland Turner et al., 2014; Littler et al., 2014; Sexton et al., 2011; Westerhold & Röhl, 2009; Westerhold et al., 2011, 2018), our benthic records spanning the Late Maastrichtian to Early Eocene from ODP Site 1262 are characterized by the existence of a strong imprint of orbital cyclicity (Figure 6; Figure 7). The presence of peaks of spectral power at the long (405-kyr) and short (100-kyr) eccentricity bands in both our orbitally-tuned $\delta^{13}C_{benthic}$ (Figure 7a) and $\delta^{18}O_{benthic}$ (Figure 7b) data suggests that changes in climate and the carbon cycle were paced predominantly by an eccentricity beat through modulation of precession. The weakness of high-latitude forcing in this warm greenhouse world, as suggested previously (Littler et al., 2014; Zeebe et al., 2017), is confirmed by the weak expression of 41 kyr-paced obliquity in both records (Figure 7a,b). This conclusion is consistent with our estimates of generally warm ocean bottom water temperatures of ~7–14°C (Figure 2f).

To examine for temporal changes in dominant periodicities over time, including the hitherto poorly studied interval encompassing the Late Maastrichtian–Middle Paleocene, we filtered our data at 405-kyr, 100-kyr and 21-kyr frequencies to identify the varying amplitude of eccentricity and precession cycles through the record (Figure 6c,d,e). We also further divided our isotope records into 5 discrete time windows (Figure 2f) based on paleoclimatic trends and ambient climate states (i.e., warming/warmer or cooling/cooler intervals), and generated Multi-Taper Method (MTM) power spectra for each interval (Figure 8). Lastly, we generated evolutionary wavelet spectra for the complete $\delta^{13}C_{benthic}$ (Figure 9a) and $\delta^{18}O_{benthic}$ (Figure 9b) records. Long and short eccentricity have the greatest concentration of spectral power within the Early Paleocene (64–61.25 Ma) and Late Paleocene–Early Eocene (58.75–52.35 Ma) time slices in both $\delta^{13}C_{benthic}$ and $\delta^{18}O_{benthic}$ (Figure 8b,d,e; Figure 9), which may be expected given larger amplitude variations within the 405-kyr and 100-kyr filters corresponding to larger hyperthermal events within our record (Figure 6c,d). By contrast,

more significant power is concentrated in the $\delta^{13}C_{benthic}$ record at 19–23 kyr frequencies during the Late Maastrichtian–Early Paleocene (67.0–64.0 Ma) time slice (Figure 8a). The 21-kyr filter (Figure 6e) and wavelet spectrum (Figure 9a) show that this amplified precession cyclicity occurs exclusively during the Late Maastrichtian, with an abrupt decrease in power across the K/Pg boundary. This feature is also present in the elemental Fe record, especially during the LMWE (Figure 2g), suggesting amplified carbon cycle sensitivity to precession during this Late Maastrichtian greenhouse event (Barnet et al., 2017). On the other hand, the Late Maastrichtian interval characterized by amplified precession cyclicity is also characterized by significantly higher sedimentation rates than the rest of the record (Figure 2h), therefore the apparent amplified precession signal may simply reflect weaker bioturbational smoothing within this part of the record. Interestingly, and in contrast to most of the record, there are also peaks in spectral power close to 41-kyr obliquity in the Late Maastrichtian–Early Paleocene portion of our record (Figure 8a,b), which may indicate a more significant role of high-latitude insolation forcing on global climate during this period characterized by the coolest climates within the record. Based on comparable $\delta^{18}O$-derived Southern Ocean temperatures during the Maastrichtian to those during the Late Eocene, when full-scale Antarctic glaciation was initiated, Huber et al. (2018) suggested the possible build-up of small ephemeral ice sheets on Antarctica during the Maastrichtian. However, the development of ice sheets during the Cretaceous remains a controversial topic and direct evidence for glaciation (e.g., unequivocal ice rafted debris) is still lacking.

3.4.2 Phasing between climate and the carbon cycle

Cross spectral analysis of the complete ODP Site 1262 $\delta^{18}O_{benthic}$ and $\delta^{13}C_{benthic}$ records (Figure 7c), and of their five discrete time windows (Figure 10), is used to characterize the phasing of orbital-scale climate and carbon cycle variations during the Late Maastrichtian–Early Eocene. Across the entire record, changes in the carbon cycle ($\delta^{13}C_{benthic}$) lag changes in climate ($\delta^{18}O_{benthic}$) by ~22.8 ±5.7 kyr at the 405-kyr band, ~4.5 ± 2.2 kyr at the 125-kyr band, and ~3 ± 0.7 kyr at the 95-kyr band, but within error, are almost in phase at precession frequencies (19–23 kyr; Figure 7c). These observations suggest that changes in orbital configuration, namely eccentricity modulation of precession, were sufficient to induce deep-sea warming. This initial warming was amplified via a positive feedback by the release of isotopically light carbon from temperature-sensitive (e.g., biogenic $CH_4$ or high-latitude permafrost) or climate-sensitive (e.g., low-latitude peat) stocks (DeConto et al., 2012; Dickens, 2003; Kurtz et al., 2003; Zachos et al., 2010).

We observe a comparable lag ($\delta^{13}C_{benthic}$ lagging $\delta^{18}O_{benthic}$) at the 405-kyr frequency within the Late Maastrichtian–Early Paleocene (~23.0 ± 11.5 kyr; Window 1), Early Paleocene (~22.0 ± 4.8 kyr; Window 2) and Early Eocene (~25.1 ± 5.0 kyr; Window 5) time slices, with smaller lags of 0.7–5.3 ± 0.7–5.4 kyr within the 100-kyr band (Figure 10a,b,e). We dismiss an apparent 7.3 ± 14.6 kyr lag of $\delta^{18}O_{benthic}$ behind $\delta^{13}C_{benthic}$ in the Late Paleocene Window 4 (Figure 10d), since phasing at the 405-kyr frequency is less coherent and uncertainty is much greater (± 14.6 kyr) within that window compared to the other time slices. The lower level of coherency during Window 4 may be related to a temporary decoupling between the carbon and oxygen isotope records at the 405-kyr frequency within the older portion of this time window at ~58.5 Ma (Figure 6c). The similar lag between the warmest climate characterized by the highest atmospheric $pCO_2$ levels within the record, the Early Eocene (Window 5), and the coolest, the Late Maastrichtian (Window 1), suggests a lack of sensitivity to ambient climate state, at least within the relatively warm and predominantly ice-free climatic range defined within this time interval.

3.5 Placing the hyperthermal events into an orbital cyclostratigraphic framework

The majority of Paleogene hyperthermals and smaller climatic perturbations occur during maxima in the 405-kyr eccentricity cycle (Figure 2b; Figure 6a), when Earth's orbit around the Sun was most elliptical, leading to an enhanced expression of the two 100-kyr cycles coeval with the 405-kyr maximum. The majority of the climatic perturbations during the Paleocene–Eocene are therefore characteristically double-spiked, such as ETM2-H2 and I1-I2 of the Early Eocene, or the LDE and Middle C27r events of the Early Paleocene (Figure 6). Variations in orbital eccentricity have little effect on the total amount of solar radiation received by Earth's surface, but these cycles do modify the difference between perihelion temperatures (when Earth passes closest to the Sun) and aphelion temperatures (when Earth is farthest from the Sun), which will be greatest during eccentricity maxima (Laskar et al., 2011). Precession cycles can therefore be significantly amplified during eccentricity maxima, which enhances seasonal contrast and has the potential to push temperature- or climate-sensitive carbon reservoirs over a critical threshold leading to their catastrophic release. Due to the double-spiked nature of many hyperthermals, the carbon source cannot have been completely depleted during the first event, in order to generate the second, typically slightly smaller event, less than 100 kyr later. Furthermore, such a short time period between events supports the release of carbon from a dynamic reservoir which could be replenished quickly, arguing against carbon stores characterized by long refueling times such as biogenic methane hydrates as the source for these cyclic orbitally-paced hyperthermals.

The length and resolution of the new benthic records also allow us to examine whether the frequency and magnitude of hyperthermal events and smaller climatic perturbations of the early Paleogene were sensitive to the low frequency orbital cycles, e.g., very long eccentricity (2.4 million years) or long-obliquity (1.2 million years), which was not possible with the previously published shorter records (Littler et al., 2014). An apparent concentration of spectral power corresponding to the long-obliquity (1200 kyr) band on the MTM plots of the entire Late Maastrichtian– Early Eocene record (Figure 7a,b) could suggest some long-obliquity modulation during this time, although power at this frequency could be an artefact as it is a multiple of the 405-kyr eccentricity cycle. We consider a strong role for long-obliquity forcing on climate and the carbon cycle to be very unlikely during this time, since there is very little spectral power concentrated within the 41-kyr band (Figure 7a,b). We see no such peak corresponding to the very long eccentricity cycle on the MTM plots (Figure 7a,b); however, comparison of the La2010b orbital solution at the 2.4 million year band reveals that many of the smaller hyperthermals and climatic perturbations of the Early–Middle Paleocene appear to cluster close to or during maxima in the very long eccentricity cycle (Figure 6a). This relationship does not, however, appear to hold true for the larger hyperthermals of the Late Paleocene–Early Eocene, when lower amplitude cyclicity is evident within the 2.4 million year band in the La2010b orbital solution (Figure 6a). More likely, sensitivity to 405-kyr eccentricity maxima increased during the generally warmer background climate of the Late Paleocene–Early Eocene, in response to the second phase of NAIP volcanism (Figure 2f,i), thereby masking the expression of low amplitude 2.4 million year cycles during this time. Increased climate and carbon cycle sensitivity to orbital forcing has been previously noted during the high $pCO_2$ greenhouse world of the LMWE, associated with Deccan Traps volcanism (Barnet et al., 2017). Double-spiked hyperthermals of a larger magnitude than those of the Paleocene are characteristic of every 405-kyr eccentricity maxima of the Early Eocene from ~54 Ma, i.e., commencing with ETM-2/H2 (Figure 2b; Figure 6a), further suggesting the release of carbon from a dynamic reservoir with a short refueling time. This period was characterized by the warmest background bottom water temperatures at ODP Site 1262 of the entire time period considered here (~12–14°C; Figure 2f), suggesting that increased carbon cycle and climate sensitivity to orbital forcing also

occurred within the warm greenhouse, high $pCO_2$ world of the Late Paleocene and especially during the Early Eocene, during the onset of the Early Eocene Climatic Optimum (EECO; ~53–49 Ma; Westerhold et al., 2018). Clearly, caution should be emphasized when interpreting the significance of longer-term (>1 million year) cycles, including the apparent broad swathe of spectral power concentrated between ~1.0–2.4 million year frequencies on the evolutionary wavelet spectra (Figure 9a,b), due to the possible distorting effects of pre-spectral analysis detrending, which specifically removes long-term (tectonic-scale) trends in order to amplify orbital-scale cyclicity (Zeebe et al., 2017; see Supporting Information).

Whilst the majority of hyperthermals and smaller climatic perturbations appear to be paced by eccentricity, the LMWE and PETM appear to represent notable exceptions, as their inceptions do not occur during 405-kyr eccentricity maxima and they lack the characteristic orbitally-paced double spike of most other hyperthermals (Figure 6a,b,f). Even though the peak of these events may be broadly in phase with a 100-kyr eccentricity maximum (Barnet et al., 2017; Zachos et al., 2010), they are unlikely to have been triggered solely by orbital forcing. Deccan Traps volcanism and the second phase of NAIP volcanism likely represent important non-orbital triggers for the LMWE and PETM, respectively (Barnet et al., 2017; Gutjahr et al., 2017; Renne et al., 2015; Schoene et al., 2015; Sinton & Duncan, 1998; Fig. 2h). The potential release of significant quantities of thermogenic methane during extrusion of NAIP volcanism subaqueously into marine organic-rich shales may also help to explain the significantly greater magnitude of the PETM, compared to other Early Paleogene hyperthermals (Gutjahr et al., 2017; Svensen et al., 2004). Similarly, the first phase of NAIP volcanism temporally coincides with three consecutive orbitally-paced climate and carbon cycle perturbations, the Latest Danian Event (LDE), Lower Chron 26r event, and Danian/Selandian Transition Event (D/STE; Sinton & Duncan, 1998). NAIP volcanism may have also played a role in the larger magnitude of these events compared to others of the Early–Middle Paleocene, due to elevated background global temperatures and increased sensitivity to orbital forcing (Figure 2b,i).

## 4 Conclusions

We present new high-resolution South Atlantic benthic isotope records spanning the Late Maastrichtian to Early Eocene, documenting the evolution of the carbon cycle and climate in unprecedented detail. We show that the Early Paleocene Dan-C2 event does not represent a typical global hyperthermal due to the lack of evidence for significant warming and carbonate dissolution in the bottom waters of the South Atlantic and elsewhere, although it may have a regional climate and carbon cycle expression in the surface ocean of the mid-latitude Atlantic and Tethys. Comparison to published lower resolution records from the equatorial Pacific suggests a broadly synchronous evolution in carbon cycle and climate between the Atlantic and Pacific oceans on multi-million year, and even orbital timescales. Spectral analysis of these paired $\delta^{13}C_{benthic}$ and $\delta^{18}O_{benthic}$ records document long (405-kyr) and short (100-kyr) eccentricity as the dominant pacemakers of the climate and carbon cycle dynamics during the Late Maastrichtian to Early Eocene, through modulation of precession. Perturbations to the global carbon cycle lag changes to global climate during this time, suggesting that temperature-sensitive light carbon was released as a positive feedback to an initial warming induced by changes in orbital configuration. The frequency of hyperthermal events suggests that isotopically light carbon was periodically released from a dynamic reservoir which could be replenished quickly, arguing against carbon stores characterized by long refueling times such as biogenic methane hydrates as the source for these cyclic orbitally-paced hyperthermals. By placing all known hyperthermals into a cyclostratigraphic framework, we identify that all occur during maxima in the 405-kyr cycle and appear to be orbitally-paced, with the exception of the PETM and LMWE, which are likely to have been

triggered or augmented by LIP volcanism. Furthermore, whilst many hyperthermal events of the Early–Middle Paleocene appear to cluster around maxima in the 2.4 million year modulation of eccentricity, the larger hyperthermal events of the Late Paleocene–Early Eocene occur during almost every 405-kyr eccentricity maximum, potentially due to a relatively minor influence of the 2.4 million year eccentricity cycle during this time, coupled with heightened carbon cycle and climate sensitivity to orbital forcing in the high $pCO_2$ greenhouse world during and following the second phase of NAIP volcanism.

**Acknowledgments, Samples, and Data**

The new Early–Middle Paleocene benthic $\delta^{13}C$ and $\delta^{18}O$ data were funded by the Natural Environment Research Council (NERC) Isotope Geosciences Facility at the British Geological Survey (IP-1581–1115), awarded to James Barnet and Kate Littler. Financial support for this research was also provided by the Deutsche Forschungsgemeinschaft (DFG) to Ursula Röhl and Thomas Westerhold, and by NSF grant OCE-1658017 to James Zachos. We thank the Bremen Core Repository for allowing us to collect the required samples, and Hilary Sloane for technical support at the NERC Isotope Geosciences Facility. We thank Dana Royer for providing the raw $pCO_2$ data, thus allowing us to recalibrate estimates based on the pedogenic carbonate proxy. Lastly, we thank two anonymous reviewers for their constructive comments which helped to improve the manuscript. The complete benthic $\delta^{13}C$ and $\delta^{18}O$ dataset underpinning this manuscript, along with additional % coarse fraction data generated across the Dan-C2 event and our compilation of published and recalibrated atmospheric $pCO_2$ estimates, are archived in the PANGAEA database (https://doi.pangaea.de/10.1594/PANGAEA.884588).

**References**

Agnini, C., Fornaciari, E., Raffi, I., Rio, D., Röhl, U., & Westerhold, T. (2007). High-resolution nannofossil biochronology of middle Paleocene to early Eocene at ODP Site 1262: Implications for calcareous nannoplankton evolution. *Marine Micropaleontology*, *64*(3–4), 215–248. https://doi.org/10.1016/j.marmicro.2007.05.003.

Anagnostou, E., John, E. H., Edgar, K. M., Foster, G. L., Ridgwell, A., Inglis, G. N., et al. (2016). Changing atmospheric $CO_2$ concentration was the primary driver of early Cenozoic climate. *Nature*, *533*(7603), 380–384. https://doi.org/10.1038/nature17423.

Arenillas, I., Molina, E., Ortiz, S., & Schmitz, B. (2008). Foraminiferal and $\delta^{13}C$ isotopic event-stratigraphy across the Danian-Selandian transition at Zumaya (northern Spain): Chronostratigraphic implications. *Terra Nova*, *20*(1), 38–44. https://doi.org/10.1111/j.1365-3121.2007.00784.x.

Barclay, R. S., & Wing, S. L. (2016). Improving the Ginkgo $CO_2$ barometer: Implications for the early Cenozoic atmosphere. *Earth and Planetary Science Letters*, *439*, 158–171. https://doi.org/10.1016/j.epsl.2016.01.012.

Barnet, J. S. K., Littler, K., Kroon, D., Leng, M. J., Westerhold, T., Rohl, U., & Zachos, J. C. (2017). A new high-resolution chronology for the late Maastrichtian warming event: Establishing robust temporal links with the onset of Deccan volcanism. *Geology*, *46*(2), 147–150. https://doi.org/10.1130/G39771.1.

Batenburg, S. J., Voigt, S., Friedrich, O., Osborne, A. H., Bornemann, A., Klein, T., et al. (2018). Major intensification of Atlantic overturning circulation at the onset of Paleogene greenhouse warmth. *Nature Communications*, *9*(1), 4954. https://doi.org/10.1038/s41467-018-07457-7.

Beerling, D. J., Lomax, B. H., Royer, D. L., Upchurch, G. R., & Kump, L. R. (2002). An atmospheric $pCO_2$ reconstruction across the Cretaceous–Tertiary boundary from leaf

megafossils. *PNAS, 99*(12), 7836–7840. https://doi.org/10.1073/pnas.122573099.
Beerling, D. J., Fox, A., & Anderson, C. W. (2009). Quantitative uncertainty analyses of ancient atmospheric $CO_2$ estimates from fossil leaves. *American Journal of Science, 309*(9), 775-787. https://doi.org/10.2475/09.2009.01.
Bemis, B. E., Spero, H. J., Bijma, J., & Lea, D. W. (1998). Reevaluation of the oxygen isotopic composition of planktonic foraminifera: Experimental results and revised paleotemperature equations. *Paleoceanography*, *13*(2), 150–160. https://doi.org/10.1029/98PA00070.
Bice, K. L., Barron, E. J., & Peterson, W. H. (1997). Continental runoff and early Cenozoic bottom-water sources. *Geology*, *25*(10), 951–954. https://doi.org/10.1130/0091-7613(1997)025<0951:CRAECB>2.3.CO;2.
Birch, H. S., Coxall, H. K., & Pearson, P. N. (2012). Evolutionary ecology of Early Paleocene planktonic foraminifera: size, depth habitat and symbiosis. *Paleobiology, 38*(3), 374–390. https://doi.org/10.1666/11027.1.
Birch, H., Coxall, H. K., Pearson, P. N., Kroon, D., & O'Regan, M. (2013). Planktonic foraminifera stable isotopes and water column structure: Disentangling ecological signals. *Marine Micropaleontology*, *101*, 127–145. https://doi.org/10.1016/j.marmicro.2013.02.002.
Birch, H. S., Coxall, H. K., Pearson, P. N., Kroon, D., & Schmidt, D. N. (2016). Partial collapse of the marine carbon pump after the Cretaceous-Paleogene boundary. *Geology*, *44*(4), 287–290. https://doi.org/10.1130/G37581.1.
Bornemann, A., Schulte, P., Sprong, J., Steurbaut, E., Youssef, M., & Speijer, R. P. (2009). Latest Danian carbon isotope anomaly and associated environmental change in the southern Tethys (Nile Basin, Egypt). *Journal of the Geological Society*, *166*, 1135–1142. https://doi.org/10.1144/0016-76492008-104.
Bowles, J. (2006). Data report: Revised magnetostratigraphy and magnetic mineralogy of sediments from Walvis Ridge, Leg 208. In D. Kroon, J. C. Zachos, C. Richter (Eds.), *Proceedings of the Ocean Drilling Program, Scientific Results* (Vol. 208, pp. 1–24). College Station, Texas: Ocean Drilling Program. https://doi.org/10.2973/odp.proc.sr.208.206.2006.
Breecker, D. O., Sharp, Z. D., & McFadden, L. D. (2010). Atmospheric $CO_2$ concentrations during ancient greenhouse climates were similar to those predicted for A.D. 2100. *PNAS*, *107*(2), 576–580. https://doi.org/10.1073/pnas.0902323106.
Cerling, T. E. (1999). Stable carbon isotopes in palaeosol carbonates. In M. Thiry & R. Simon-Coincon (Eds.), *Palaeoweathering, palaeosurfaces and related continental deposits, International Association of Sedimentologists Special Publication* (Vol. 27, pp. 43–60). https://doi.org/10.1002/9781444304190.ch2.
Coccioni, R., Frontalini, F., Bancalà, G., Fornaciari, E., Jovane, L., & Sprovieri, M. (2010). The Dan-C2 hyperthermal event at Gubbio (Italy): Global implications, environmental effects, and cause(s). *Earth and Planetary Science Letters*, *297*(1), 298–305. https://doi.org/10.1016/j.epsl.2010.06.031.
Cramer, B. S., Toggweiler, J. R., Wright, J. D., Katz, M. E., & Miller, K. G. (2009). Ocean overturning since the Late Cretaceous: Inferences from a new benthic foraminiferal isotope compilation. *Paleoceanography*, *24*(4), PA4216. https://doi.org/10.1029/2008PA001683.
Cubasch, U., Wuebbles, D., Chen, D., Facchini, M. C., Frame, D., Mahowald, N., & Winther, J-G. (2013). Introduction. In T. F. Stocker, D. Qin, G-K. Plattner, M. Tignor, S. K. Allen, J. Boschung et al., (Eds.), *Climate change 2013: The physical science basis*. *Contribution of Working Group I to the Fifth Assessment Report of the Intergovernmental Panel on Climate Change* (pp. 119–158). Cambridge, UK:

Cambridge University Press.
Cui, Y., & Schubert, B.A. (2016). Quantifying uncertainty of past $pCO_2$ determined from changes in C3 plant carbon isotope fractionation. *Geochimica et Cosmochimica Acta*, *172*, 127–138. https://doi.org/10.1016/j.gca.2015.09.032.
Cui, Y., & Schubert, B.A. (2017). Atmospheric $pCO_2$ reconstructed across five early Eocene global warming events. *Earth and Planetary Science Letters*, *478*, 225–233. https://doi.org/10.1016/j.epsl.2017.08.038.
Dameron, S. N., Leckie, R. M., Clark, K., MacLeod, K. G., Thomas, D. J., & Lees, J. A. (2017). Extinction, dissolution, and possible ocean acidification prior to the Cretaceous/Paleogene (K/Pg) boundary in the tropical Pacific. *Palaeogeography, Palaeoclimatology, Palaeoecology*, *485*, 433–454. https://doi.org/10.1016/j.palaeo.2017.06.032.
DeConto, R. M., Galeotti, S., Pagani, M., Tracy, D., Schaefer, K., Zhang, T., et al. (2012). Past extreme warming events linked to massive carbon release from thawing permafrost. *Nature*, *484*(7392), 87–91. https://doi.org/10.1038/nature10929.
Demicco, R. V., Lowenstein, T. K., & Hardie, L. A. (2003). Atmospheric $pCO_2$ since 60 Ma from records of seawater pH, calcium, and primary carbonate mineralogy. *Geology*, *31*(9), 793–796. https://doi.org/10.1130/G19727.1.
Deprez, A., Jehle, S., Bornemann, A. E., & Speijer, R.P. (2017). Differential response at the seafloor during Palaeocene and Eocene ocean warming events at Walvis Ridge, Atlantic Ocean (ODP Site 1262). *Terra Nova*, *29*(1), 71–76. https://doi.org/10.1111/ter.12250.
D'Hondt, S., Donaghay, P., Zachos, J. C., Luttenberg, D., & Lindinger, M. (1998). Organic carbon fluxes and ecological recovery from the Cretaceous-Tertiary mass extinction. *Science*, *282*(5387), 276–279. https://doi.org/10.1126/science.282.5387.276.
Dickens, G. R. (2003). Rethinking the global carbon cycle with a large, dynamic and microbially mediated gas hydrate capacitor. *Earth and Planetary Science Letters*, *213*(3–4), 169–183. https://doi.org/10.1016/S0012-821X(03)00325-X.
Dinarès-Turell, J., Westerhold, T., Pujalte, V., Röhl, U., & Kroon, D. (2014). Astronomical calibration of the Danian stage (Early Paleocene) revisited: Settling chronologies of sedimentary records across the Atlantic and Pacific Oceans. *Earth and Planetary Science Letters*, *405*, 119–131. https://doi.org/10.1016/j.epsl.2014.08.027.
Edgar, K. M., Pälike, H., & Wilson, P.A. (2013). Testing the impact of diagenesis on the $\delta^{18}O$ and $\delta^{13}C$ of benthic foraminiferal calcite from a sediment burial depth transect in the equatorial Pacific. *Paleoceanography*, *28*(3), 468–480. https://doi.org/10.1002/palo.20045.
Fletcher, B. J., Brentnall, S. J., Anderson, C. W., Berner, R. A., & Beerling, D. J. (2008). Atmospheric carbon dioxide linked with Mesozoic and early Cenozoic climate change. *Nature Geoscience*, *1*(1), 43–48. https://doi.org/10.1038/ngeo.2007.29.
Gehler, A., Gingerich, P. D., & Pack, A. (2016). Temperature and atmospheric $CO_2$ concentration estimates through the PETM using triple oxygen isotope analysis of mammalian bioapatite. *PNAS*, *113*(28), 7739–7744. https://doi.org/10.1073/pnas.1518116113.
Gutjahr, M., Ridgwell, A., Sexton, P.F., Anagnostou, E., Pearson, P. N., Pälike, H., et al. (2017). Very large release of mostly volcanic carbon during the Palaeocene – Eocene Thermal Maximum. *Nature*, *548*(7669), 573–577. https://doi.org/10.1038/nature23646.
Hilting, A. K., Kump, L. R., & Bralower, T. J. (2008). Variations in the oceanic vertical carbon isotope gradient and their implications for the Paleocene–Eocene biological pump. *Paleoceanography*, *23*(3), PA3222. https://doi.org/10.1029/2007PA001458.
Huang, C., Retallack, G. J., Wang, C., & Huang, Q. (2013). Paleoatmospheric $pCO_2$ fluctuations across the Cretaceous-Tertiary boundary recorded from paleosol carbonates

in NE China. *Palaeogeography, Palaeoclimatology, Palaeoecology*, *385*, 95–105. https://doi.org/10.1016/j.palaeo.2013.01.005.

Huber, B. T., MacLeod, K. G., Watkins, D. K., & Coffin, M. F. (2018). The rise and fall of the Cretaceous Hot Greenhouse climate. *Global and Planetary Change*, *167*, 1–23. https://doi.org/10.1016/j.gloplacha.2018.04.004.

Husson, D., Galbrun, B., Laskar, J., Hinnov, L. A., Thibault, N., Gardin, S., & Locklair, R. E. (2011). Astronomical calibration of the Maastrichtian (Late Cretaceous). *Earth and Planetary Science Letters*, *305*(3–4), 328–340. https://doi.org/10.1016/j.epsl.2011.03.008.

Katz, M. E., Katz, D. R., Wright, J. D., Miller, K. G., Pak, D. K., Shackleton, N. J., & Thomas, E. (2003). Early Cenozoic benthic foraminiferal isotopes: species reliability and inter-species correction factors. *Paleoceanography*, *18*(2), 1024. https://doi.org/10.1029/2002PA000798.

Kim, S.-T., & O'Neil, J. R. (1997). Equilibrium and nonequilibrium oxygen isotope effects in synthetic carbonates. *Geochimica et Cosmochimica Acta*, *61*(16), 3461–3475.

Kirtland Turner, S., Sexton, P. F., Charles, C. D., & Norris, R. D. (2014). Persistence of carbon release events through the peak of early Eocene global warmth. *Nature Geoscience*, *7*(10), 8–11. https://doi.org/10.1038/NGEO2240.

Koch, P. L., Zachos, J. C., & Gingerich, P. D. (1992). Correlation between isotope records in marine and continental carbon reservoirs near the Palaeocene/Eocene boundary. *Nature*, *358*(6384), 319–322. https://doi.org/10.1038/358319a0.

Komar, N., Zeebe, R. E., & Dickens, G. R. (2013). Understanding long-term carbon cycle trends: The late Paleocene through the early Eocene. *Paleoceanography*, *28*(4), 650–662. https://doi.org/10.1002/palo.20060.

Kroon, D., Zachos, J. C., & Leg 208 Scientific Party. (2007). Leg 208 Synthesis: Cenozoic climate cycles and excursions. In D. Kroon, J. C. Zachos, & C. Richter (Eds.), *Proceedings of the Ocean Drilling Program, Scientific Results* (Vol. 208, pp. 1–55). College Station, Texas: Ocean Drilling Program. https://doi.org/10.2973/odp.proc.sr.208.201.2007.

Kuhnt, W. (1990). Agglutinated foraminifera of western Mediterranean Upper Cretaceous pelagic limestones (Umbrian Apennines, Italy, and Betic Cordillera, Southern Spain. *Micropaleontology*, *36*(4), 297–330. https://doi.org/10.2307/1485473.

Kurtz, A., Kump, L. R., Arthur, M. A., Zachos, J. C., & Paytan, A. (2003). Early Cenozoic decoupling of the global carbon and sulfur cycles. *Paleoceanography*, *18*(4), 1090. https://doi.org/10.1029/2003PA000908.

Laskar, J., Fienga, A., Gastineau, M., & Manche, H. (2011). La2010: a new orbital solution for the long-term motion of the Earth. *Astronomy & Astrophysics*, *532*, A89. https://doi.org/10.1051/0004-6361/201116836.

Lauretano, V., Littler, K., Polling, M., Zachos, J. C., & Lourens, L. J. (2015). Frequency, magnitude and character of hyperthermal events at the onset of the Early Eocene Climatic Optimum. *Climate of the Past*, *11*(10), 1313–1324. https://doi.org/10.5194/cp-11-1313-2015.

Lourens, L. J., Sluijs, A., Kroon, D., Zachos, J. C., Thomas, E., Röhl, U., et al. (2005). Astronomical pacing of late Palaeocene to early Eocene global warming events. *Nature*, *435*(7045), 1083–1087. https://doi.org/10.1038/nature03814.

Lunt, D. J., Valdes, P. J., Dunkley Jones, T., Ridgwell, A., Haywood, A. M., Schmidt, D. N., et al. (2010). $CO_2$-driven ocean circulation changes as an amplifier of Paleocene-Eocene thermal maximum hydrate destabilization. *Geology*, *38*(10), 875–878. https://doi.org/10.1130/G31184.1.

McCarren, H., Thomas, E., Hasegawa, T., Röhl, U., & Zachos, J. C. (2008). Depth

dependency of the Paleocene–Eocene carbon isotope excursion: paired benthic and terrestrial biomarker records (Ocean Drilling Program Leg 208, Walvis Ridge). *Geochemistry Geophysics Geosystems*, *9*(10), Q10008. https://doi.org/10.1029/2008GC002116.

McInerney, F. A., & Wing, S. L. (2011). The Paleocene-Eocene Thermal Maximum: A Perturbation of Carbon Cycle, Climate, and Biosphere with Implications for the Future. *Annual Review of Earth & Planetary Science*, *39*, 489–516. https://doi.org/10.1146/annurev-earth-040610-133431.

Meyers, S. R. (2012). Seeing Red in Cyclic Stratigraphy: Spectral Noise Estimation for Astrochronology. *Paleoceanography*, *27*(3), PA3228. https://doi.org/10.1029/2012PA002307.

Meyers, S. R. (2014). Astrochron: An R Package for Astrochronology. http://cran.r-project.org/package=astrochron.

Monechi, S., Reale, V., Bernaola, G., & Balestra, B. (2013). The Danian/Selandian boundary at Site 1262 (South Atlantic) and in the Tethyan region: Biomagnetostratigraphy, evolutionary trends in fasciculiths and environmental effects of the Latest Danian Event. *Marine Micropaleontology*, *98*, 28–40. https://doi.org/10.1016/j.marmicro.2012.11.002.

Nordt, L., Atchley, S., & Dworkin, S. I. (2002). Paleosol barometer indicates extreme fluctuations in atmospheric $CO_2$ across the Cretaceous-Tertiary boundary. *Geology*, *30*(8), 703–706. https://doi.org/10.1130/0091-7613(2002)030<0703:PBIEFI>2.0.CO;2.

Nordt, L., Atchley, S., & Dworkin, S. (2003). Terrestrial evidence for two greenhouse events in the latest Cretaceous. *GSA Today*, *13*(12), 4–9. https://doi.org/10.1130/1052-5173(2003)013<4:TEFTGE>2.0.CO;2.

Paillard, D., Labeyrie, L., & Yiou, P. (1996). Macintosh program performs time-series analysis. *EOS Transactions*, *77*(39), 379. https://doi.org/10.1029/96EO00259.

Panchuk, K., Ridgwell, A., & Kump, L. R. (2008). Sedimentary response to Paleocene-Eocene Thermal Maximum carbon release: A model-data comparison. *Geology*, *36*(4), 315–318. https://doi.org/10.1130/G24474A.1.

Quillévéré, F., Norris, R. D., Kroon, D., & Wilson, P. A. (2008). Transient ocean warming and shifts in carbon reservoirs during the early Danian. *Earth and Planetary Science Letters*, *265*(3), 600–615. https://doi.org/10.1016/j.epsl.2007.10.040.

Renne, P. R., Sprain, C. J., Richards, M. A., Self, S., Vanderkluysen, L., & Pande, K. (2015). State shift in Deccan volcanism at the Cretaceous-Paleogene boundary, possibly induced by impact. *Science*, *350*(6256), 76–78. https://doi.org/10.1126/science.aac7549.

Royer, D. L. (2003). Estimating latest Cretaceous and Tertiary atmospheric $CO_2$ concentration from stomatal indices. In S. L. Wing, P. D. Gingerich, B. Schmitz, & E. Thomas (Eds.), *Causes and Consequences of Globally Warm Climates in the Early Paleogene*, *Geological Society of America Special Paper* (Vol. 369, pp. 79–93). Boulder, Colorado: Geological Society of America. https://doi.org/10.1130/0-8137-2369-8.79.

Royer, D. L. (2006). $CO_2$-forced climate thresholds during the Phanerozoic. *Geochimica et Cosmochimica Acta*, *70*(23), 5665–5675. https://doi.org/10.1016/j.gca.2005.11.031.

Royer, D. L. (2014). Atmospheric $CO_2$ and $O_2$ during the Phanerozoic: tools, patterns, and impacts. *Geochemistry Treatise (Second Edition)*, *6*, 251–267. https://doi.org/10.1016/B978-0-08-095975-7.01311-5.

Royer, D. L., Berner, R. A., & Beerling, D. J. (2001a). Phanerozoic $CO_2$ change: evaluating geochemical and paleobiological approaches. *Earth-Science Reviews*, *54*(4), 349–392. https://doi.org/10.1016/S0012-8252(00)00042-8.

Royer, D. L., Wing, S. L., Beerling, D. J., Jolley, D. W., Koch, P. L., Hickey, L. J., & Berner, R. A. (2001b). Paleobotanical evidence for near present-day levels of atmospheric $CO_2$

during part of the Tertiary. *Science*, *292*(5525), 2310–2313. https://doi.org/10.1126/science.292.5525.2310.

Schoene, B., Samperton, K. M., Eddy, M. P., Keller, G., Adatte, T., Bowring, S. A., et al. (2015). U-Pb geochronology of the Deccan Traps and relation to the end-Cretaceous mass extinction. *Science*, *347*(6218), 182–184. https://doi.org/10.1126/science.aaa0118.

Schulte, P., Alegret, L., Arenillas, I., Arz, J. A., Barton, P. J., Bown, P. R., et al. (2010). The Chicxulub Asteroid Impact and Mass Extinction at the Cretaceous-Paleogene Boundary. *Science*, *327*(5970), 1214–1218. https://doi.org/10.1126/science.1177265.

Sexton, P. F., Norris, R. D., Wilson, P. A., Pälike, H., Westerhold, T., Röhl, U., et al. (2011). Eocene global warming events driven by ventilation of oceanic dissolved organic carbon. *Nature*, *471*(7338), 349–352. https://doi.org/10.1038/nature09826.

Shackleton, N. J., Hall, M. A., & Boersma, A. (1984). Oxygen and carbon isotope data from Leg 74 foraminifers. *Initial Reports of the Deep Sea Drilling Project*, *74*, 599–612. https://doi.org/10.2973/dsdp.proc.74.115.1984.

Shipboard Scientific Party. (1998). Site 1049. In R. D. Norris, D. Kroon, A. Klaus, et al. (Eds.), *Proceedings of the Ocean Drilling Program, Initial Reports* (Vol. 171B, pp. 47–92). College Station, Texas: Ocean Drilling Program. https://doi.org/10.2973/odp.proc.ir.171B.103.1998.

Shipboard Scientific Party. (2002). Site 1209. In T .J. Bralower, I. Premoli Silva, M. J. Malone, et al. (Eds.), *Proceedings of the Ocean Drilling Program, Initial Reports* (Vol. 198, pp. 1–102). College Station, Texas: Ocean Drilling Program. https://doi.org/10.2973/odp.proc.ir.198.105.2002.

Shipboard Scientific Party. (2004). Site 1262. In J. C. Zachos, D. Kroon, P. Blum, et al. (Eds.), *Proceedings of the Ocean Drilling Program, Initial Reports* (Vol. 208, pp. 1–92). College Station, Texas: Ocean Drilling Program. https://doi.org/10.2973/odp.proc.ir.208.103.2004.

Sinha, A., & Stott, L. D. (1994). New atmospheric $pCO_2$ estimates from paleosols during the late Paleocene/early Eocene global warming interval. *Global and Planetary Change*, *9*(3–4), 297–307. https://doi.org/10.1016/0921-8181(94)00010-7.

Sinton, C. W., & Duncan, R. A. (1998). $^{40}Ar$-$^{39}Ar$ ages of lavas from the southeast Greenland margin, ODP Leg 152, and the Rockall Plateau, DSDP Leg 81. In A. D. Saunders, H. C. Larsen, P. D. Clift, & S. W. Wise (Eds.), *Proceedings of the Ocean Drilling Program, Scientific Results* (Vol. 152, pp. 387–402). College Station, Texas: Ocean Drilling Program. https://doi.org/10.2973/odp.proc.sr.152.234.1998.

Slotnick, B. S., Lauretano, V., Backman, J., Dickens, G. R., Sluijs, A., & Lourens, L. (2015). Early Paleogene variations in the calcite compensation depth: new constraints using old borehole sediments from across Ninetyeast Ridge, central Indian Ocean. *Climate of the Past*, *11*(3), 473–493. https://doi.org/10.5194/cp-11-473-2015.

Stap, S., Lourens, L. J., Thomas, E., Sluijs, A., Bohaty, S., & Zachos, J. C. (2010). High-resolution deep-sea carbon and oxygen isotope records of Eocene Thermal Maximum 2 and H2. *Geology*, *38*(7), 607–610. https://doi.org/10.1130/G30777.1.

Steinthorsdottir, M., Vajda, V., & Pole, M. (2016). Global trends of $pCO_2$ across the Cretaceous – Paleogene boundary supported by the first Southern Hemisphere stomatal proxy-based $pCO_2$ reconstruction. *Palaeogeography, Palaeoclimatology, Palaeoecology*, *464*, 143–152. https://doi.org/10.1016/j.palaeo.2016.04.033.

Stott, L. D. (1992). Higher temperatures and lower oceanic $pCO_2$: A climate enigma at the end of the Paleocene Epoch. *Paleoceanography*, *7*(4), 395–404 (1992). https://doi.org/10.1029/92PA01183.

Svensen, H., Planke, S., Malthe-Sørenssen, A., Jamtveit, B., Myklebust, R., Rasmussen Eidem, T., & Rey, S. S. (2004). Release of methane from a volcanic basin as a

mechanism for initial Eocene global warming. *Nature*, *429*(6991), 542–545. https://doi.org/10.1038/nature02566.

Thomas, D. J., Bralower. T .J., & Jones, C. E. (2003). Neodymium isotopic reconstruction of late Paleocene–early Eocene thermohaline circulation. *Earth and Planetary Science Letters*, *209*(3–4), 309–322. https://doi.org/10.1016/S0012-821X(03)00096-7.

Thomas, D. J., Lyle, M., Moore, T. C. Jr., & Rea, D. K. (2008). Paleogene deepwater mass composition of the tropical Pacific and implications for thermohaline circulation in a greenhouse world. *Geochemistry, Geophysics, Geosystems*, *9*(2), Q02002. https://doi.org/10.1029/2007GC001748.

Thomas, E. (2003). Extinction and food at the seafloor: A high-resolution benthic foraminiferal record across the Initial Eocene Thermal Maximum, Southern Ocean Site 690. In S. L. Wing, P. D. Gingerich, B. Schmitz, & E. Thomas (Eds.), *Causes and Consequences of Globally Warm Climates in the Early Paleogene, Geological Society of America Special Paper* (Vol. 369, pp. 319–332). Boulder, Colorado: Geological Society of America. https://doi.org/10.1130/0-8137-2369-8.319.

Torsvik, T. H., Van der Voo, R., Preeden, U., Niocaill, C. M., Steinberger, B., Doubrovine, P. V., et al. (2012). Phanerozoic polar wander, palaeogeography and dynamics. *Earth-Science Reviews*, *114*(3–4), 325–368. https://doi.org/10.1016/j.earscirev.2012.06.007.

Van Hinsbergen, D. J. J., De Groot, L. V., Van Schaik, S. J., Spakman, W., Bijl, P. K., Sluijs, A., et al. (2015). A paleolatitude calculator for paleoclimate studies. *PLoS ONE*, *10*(6), 1–21. https://doi.org/10.1371/journal.pone.0126946.

Westerhold, T., Agnini, C., & Wilkens, R. H. (2017). Astronomical calibration of the Ypresian time scale: implications for seafloor spreading rates and the chaotic behaviour of the solar system? *Climate of the Past*, *13*(9), 1129–1152. https://doi.org/10.5194/cp-13-1129-2017.

Westerhold, T., & Röhl, U. (2009). High resolution cyclostratigraphy of the early Eocene – new insights into the origin of the Cenozoic cooling trend. *Climate of the Past*, *5*(3), 309–327. https://doi.org/10.5194/cp-5-309-2009.

Westerhold, T., Röhl, U., Donner, B., McCarren, H. K., & Zachos, J. C. (2011). A complete high-resolution Paleocene benthic stable isotope record for the central Pacific (ODP Site 1209). *Paleoceanography*, *26*(2), PA2216. https://doi.org/10.1029/2010PA002092.

Westerhold, T., Röhl, U., Donner, B., and Zachos, J. C. (2018). Global extent of Early Eocene hyperthermal events: A new Pacific benthic foraminiferal isotope record from Shatsky Rise (ODP Site 1209). *Paleoceanography and Paleoclimatology*, *33*(6), 626–642. https://doi.org/10.1029/2017PA003306.

Westerhold, T., Röhl, U., Laskar, J., Raffi, I., Bowles, J., Lourens, L. J., & Zachos, J. C. (2007). On the duration of magnetochrons C24r and C25n and the timing of early Eocene global warming events: Implications from the Ocean Drilling Program Leg 208 Walvis Ridge depth transect. *Paleoceanography*, *22*(2), PA2201. https://doi.org/10.1029/2006PA001322.

Westerhold, T., Röhl, U., Raffi, I., Fornaciari, E., Monechi, S., Reale, V., et al. (2008). Astronomical calibration of the Paleocene time. *Palaeogeography, Palaeoclimatology, Palaeoecology*, *257*(4), 377–403. https://doi.org/10.1016/j.palaeo.2007.09.016.

Zachos, J. C., & Arthur, M. A. (1986). Paleoceanography of the Cretaceous/Tertiary Boundary Event: Inferences from stable isotopic and other data. *Paleoceanography*, *1*(1), 5–26. https://doi.org/10.1029/PA001i001p00005.

Zachos, J. C., Arthur, M. A., & Dean, W. E. (1989). Geochemical evidence for suppression of pelagic marine productivity at the Cretaceous/Tertiary boundary. *Nature*, *337*(6202), 61–64, https://doi.org/10.1038/337061a0.

Zachos, J. C., Dickens, G. R., & Zeebe, R. E. (2008). An early Cenozoic perspective on

greenhouse warming and carbon-cycle dynamics. *Nature*, *451*(7176), 279–283. https://doi.org/10.1038/nature06588.

Zachos, J. C., McCarren, H., Murphy, B., Röhl, U., & Westerhold, T. (2010). Tempo and scale of late Paleocene and early Eocene carbon isotope cycles: Implications for the origin of hyperthermals. *Earth and Planetary Science Letters*, *299*(1), 242–249. https://doi.org/10.1016/j.epsl.2010.09.004.

Zachos, J. C., Pagani, M., Sloan, L., Thomas, E., & Billups, K. (2001). Trends, rhythms, and aberrations in global climate 65 Ma to present. *Science*, *292*(5517), 686–693. https://doi.org/10.1126/science.1059412.

Zachos, J. C., Röhl, U., Schellenberg, S. A., Sluijs, A., Hodell, D. A., Kelly, D. C., et al. (2005). Rapid acidification of the ocean during the Paleocene-Eocene Thermal Maximum. *Science*, *308*(5728), 1611–1615. https://doi.org/10.1126/science.1109004.

Zeebe, R. E., Westerhold, T., Littler, K., & Zachos, J. C. (2017). Orbital forcing of the Paleocene and Eocene carbon cycle. *Paleoceanography*, *32*(5), 440–465. https://doi.org/10.1002/2016PA003054.

Zeebe, R. E., Zachos, J. C., & Dickens, G. R. (2009). Carbon dioxide forcing alone insufficient to explain Palaeocene-Eocene Thermal Maximum warming. *Nature Geoscience*, *2*(8), 576–580. https://doi.org/10.1038/ngeo578.

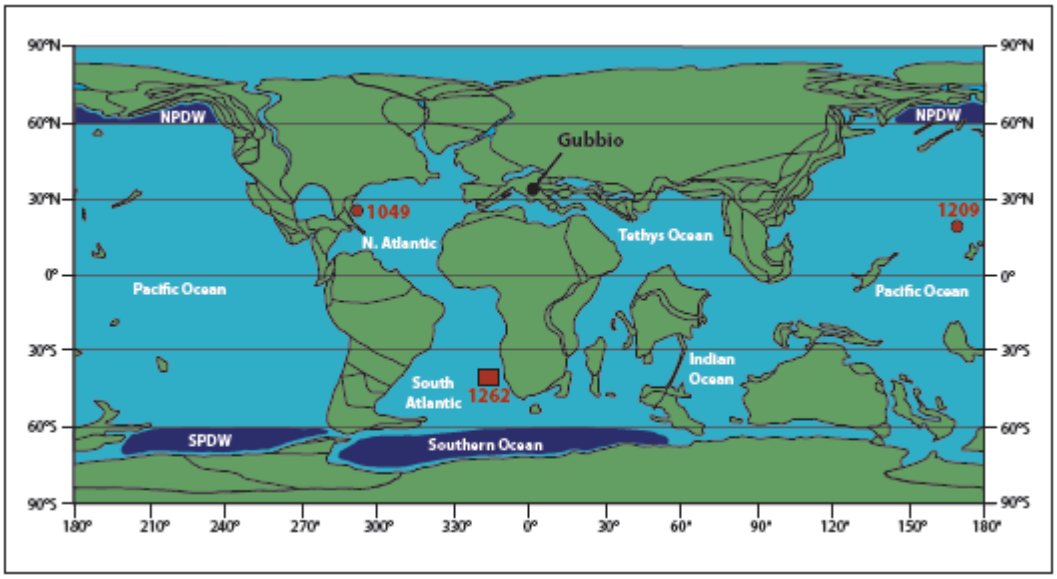


Figure 1. Paleogeographic reconstruction for the K/Pg boundary (66 Ma) and location of sites used in this study. Ocean Drilling Program sites are highlighted by red circles and labels; onshore sites by black circles and labels. Regions of deep-water formation are schematically highlighted by dark blue polygons. NPDW = North Pacific Deep Water. SPDW = South Pacific Deep Water. Adapted from Ocean Drilling Stratigraphic Network (ODSN) Paleomap Project (http://www.odsn.de/odsn/services/paleomap/paleomap.html).

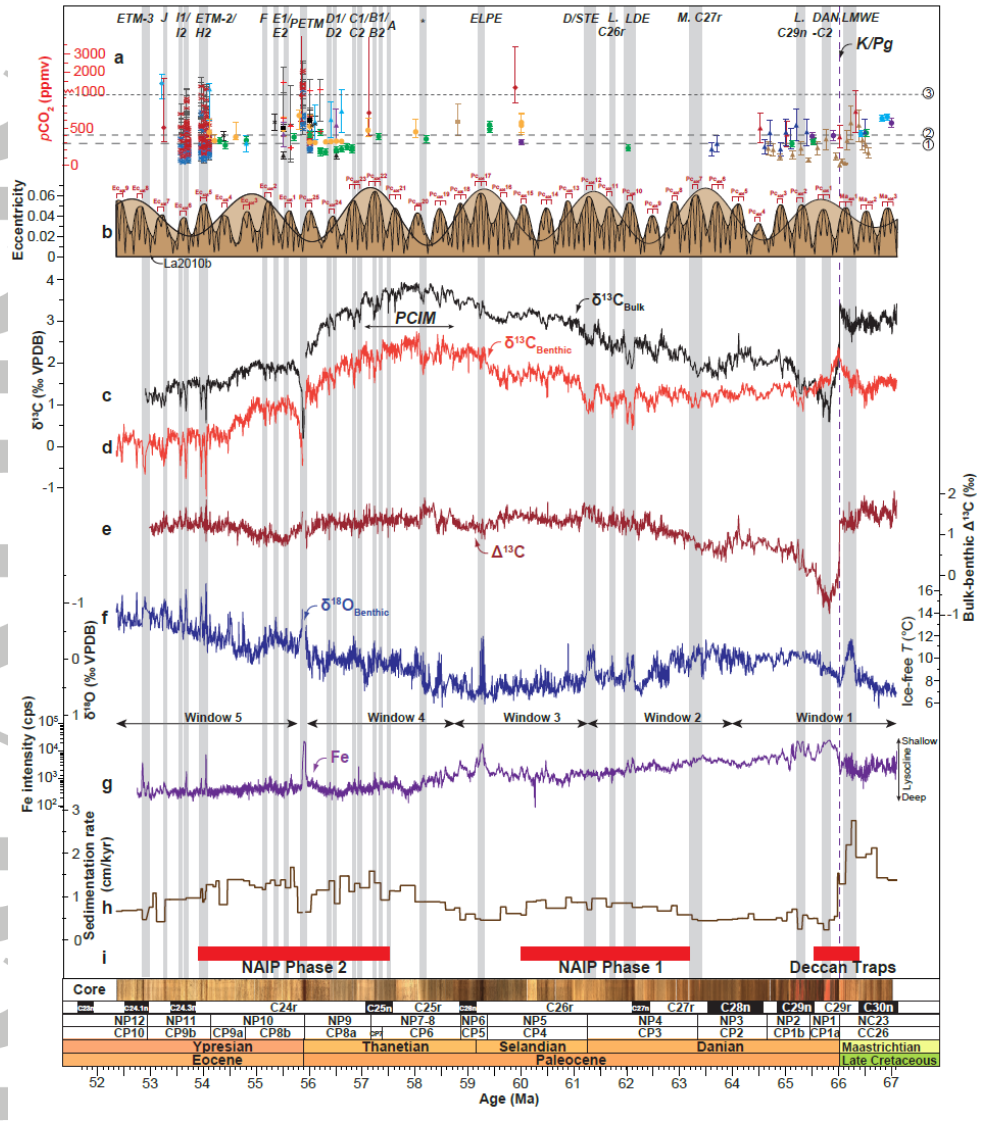


Figure 2. Recalibrated proxies for atmospheric $pCO_2$ along with stable carbon and oxygen isotope records and elemental Fe intensities from ODP Site 1262, calibrated against the updated orbitally-tuned age model. Previously described hyperthermals and smaller climatic perturbations are indicated by labelled grey bands, with the following abbreviations: LMWE – Late Maastrichtian warming event; Dan-C2 – Dan-C2 event; L. C29n – Lower Chron 29n event; M. C27r – Middle Chron 27r event; LDE – Latest Danian Event; L. C26r – Lower Chron 26r event; D/STE – Danian/Selandian Transition Event; ELPE – Early Late Paleocene Event; PETM – Paleocene-Eocene Thermal Maximum; ETM-2 – Eocene Thermal Maximum 2; ETM-3 – Eocene Thermal Maximum 3. Core photo from Shipboard Scientific Party (2004). (**a**) Recalibrated atmospheric $pCO_2$ data (see Supplementary Figure S2 for legend and literature sources). Horizontal dashed lines indicate pre-industrial (1), and 2018 (2) levels, along with the most pessimistic emission scenario (RCP8.5) for the year 2100 (3), from Cubasch et al. (2013). (**b**) La2010b orbital solution (Laskar et al., 2011), with long eccentricity (405-kyr) maxima illustrated in dark brown and the filtered ~2.4 million year modulation of eccentricity illustrated in pale brown. 405-kyr eccentricity maxima are labelled in red following the nomenclature of Husson et al. (2011) for the Maastrichtian, Dinarès-Turell et al. (2014) for the Paleocene, and Westerhold and Röhl (2009) for the Eocene. Panels **c**–**g**, new and published stable isotope and geochemical records from ODP Site 1262: (**c**) Bulk carbonate $\delta^{13}C$; (**d**) Benthic $\delta^{13}C$; (**e**) Bulk $\delta^{13}C$ to benthic $\delta^{13}C$ (representing surface to deep) gradient; (**f**) Benthic $\delta^{18}O$, with distribution of discrete time windows used in Figure 8 and Figure 10. The sources of all stable isotope data are illustrated in Supplementary Figure S2. (**g**) Elemental Fe intensity (Westerhold et al., 2007, 2008). (**h**) Sedimentation rate based on new age model. (**i**) Timing of Large Igneous Province volcanism (Renne et al., 2015; Schoene et al., 2015; Sinton & Duncan, 1998).

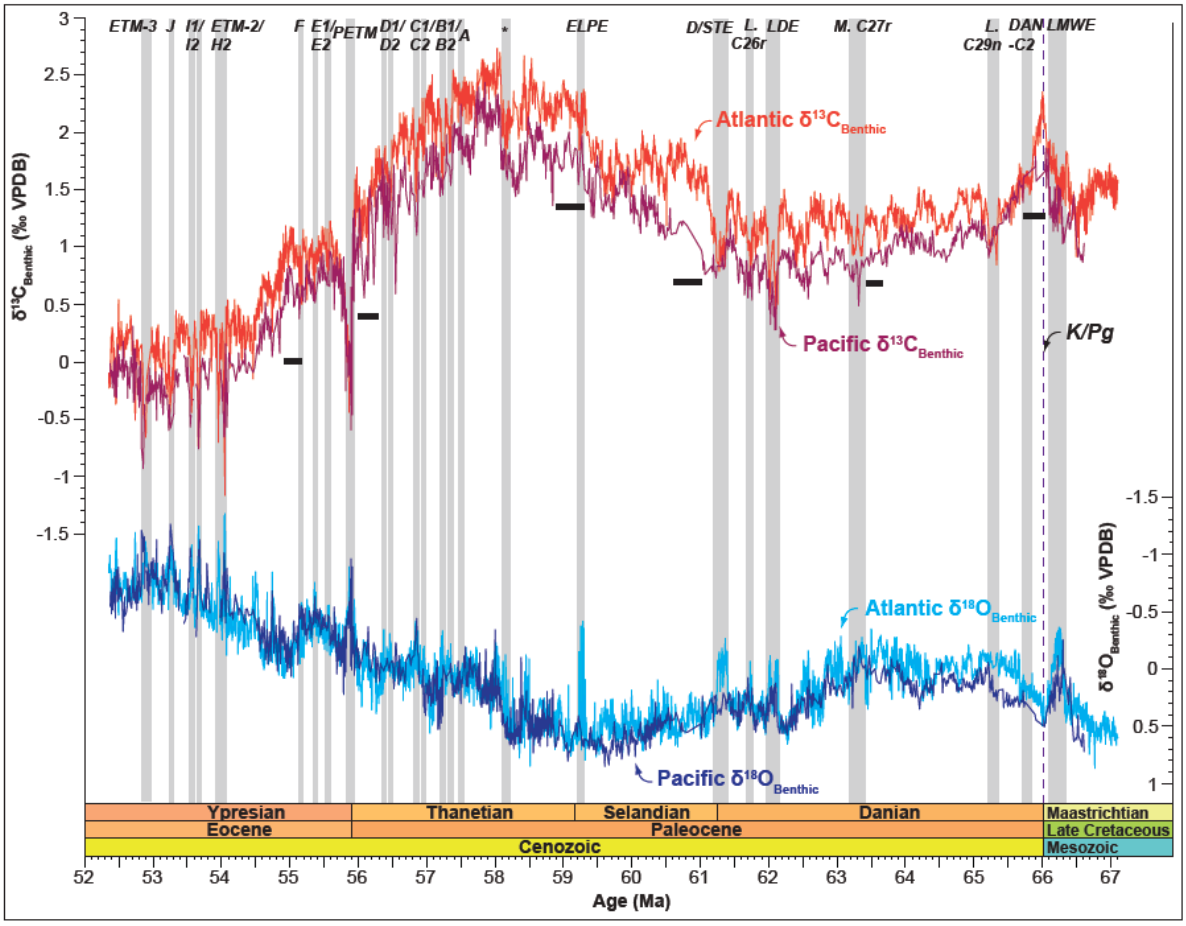


Figure 3. $\delta^{13}C_{benthic}$ and $\delta^{18}O_{benthic}$ records from ODP Site 1262 (South Atlantic) and ODP Site 1209 (equatorial Pacific; Westerhold et al., 2011, 2018), spanning the Late Maastrichtian–Early Eocene. Both datasets are calibrated to a common orbitally-tuned age model correlated to the La2010b orbital solution (Laskar et al., 2011). See Figure 1 for site locations. Condensed intervals at ODP Site 1209 are highlighted beneath the $\delta^{13}C_{benthic}$ record by black bars. Hyperthermals and smaller climatic perturbations are illustrated by labelled grey vertical bars.

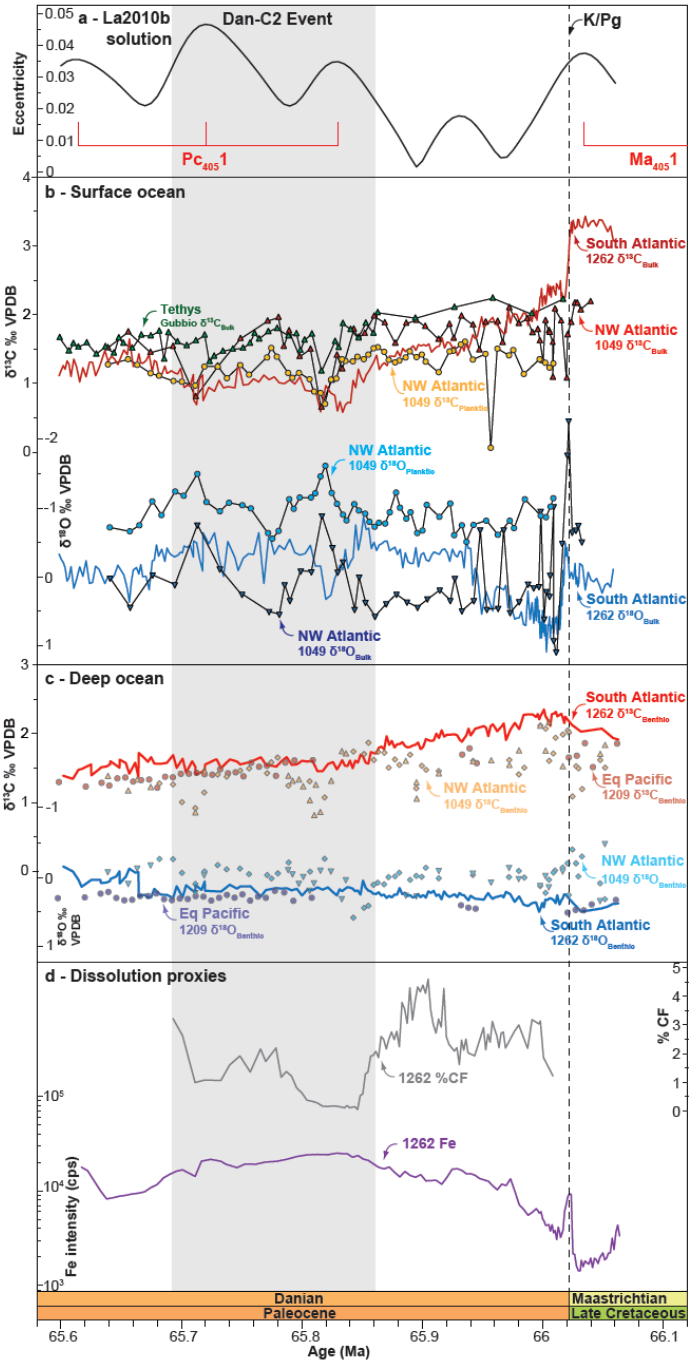


Figure 4. Compilation of stable isotope and dissolution proxy data for the Dan-C2 event, correlated to the La2010b orbital solution (Laskar et al., 2011). Locations of ODP sites and onshore outcrops are shown in Figure 1, with further details for each site listed in Table S1. (**a**) La2010b orbital solution (Laskar et al., 2011), with long eccentricity (405-kyr) maxima labelled in red following the nomenclature of Husson et al. (2011) for the Maastrichtian and Dinarès-Turell et al. (2014) for the Paleocene; (**b**) Surface planktic ($\delta^{13}C_{planktic}$ and $\delta^{18}O_{planktic}$) and bulk carbonate ($\delta^{13}C_{bulk}$ and $\delta^{18}O_{bulk}$) stable isotope data from ODP Site 1049, NW Atlantic (Quillévéré et al., 2008), along with bulk isotope data from ODP Site 1262, South Atlantic (Kroon et al., 2007) and Gubbio, Italy (Coccioni et al., 2010); (**c**) Benthic ($\delta^{13}C_{benthic}$ and $\delta^{18}O_{benthic}$) stable isotope data from ODP Site 1262, South Atlantic (Barnet et al., 2017; this study), ODP Site 1209, central Pacific (Westerhold et al., 2011) and ODP Site 1049, NW Atlantic (Quillévéré et al., 2008); (**d**) Dissolution proxy data from ODP Site 1262, with % coarse fraction (% CF; this study) and Fe intensity data (Westerhold et al., 2008).

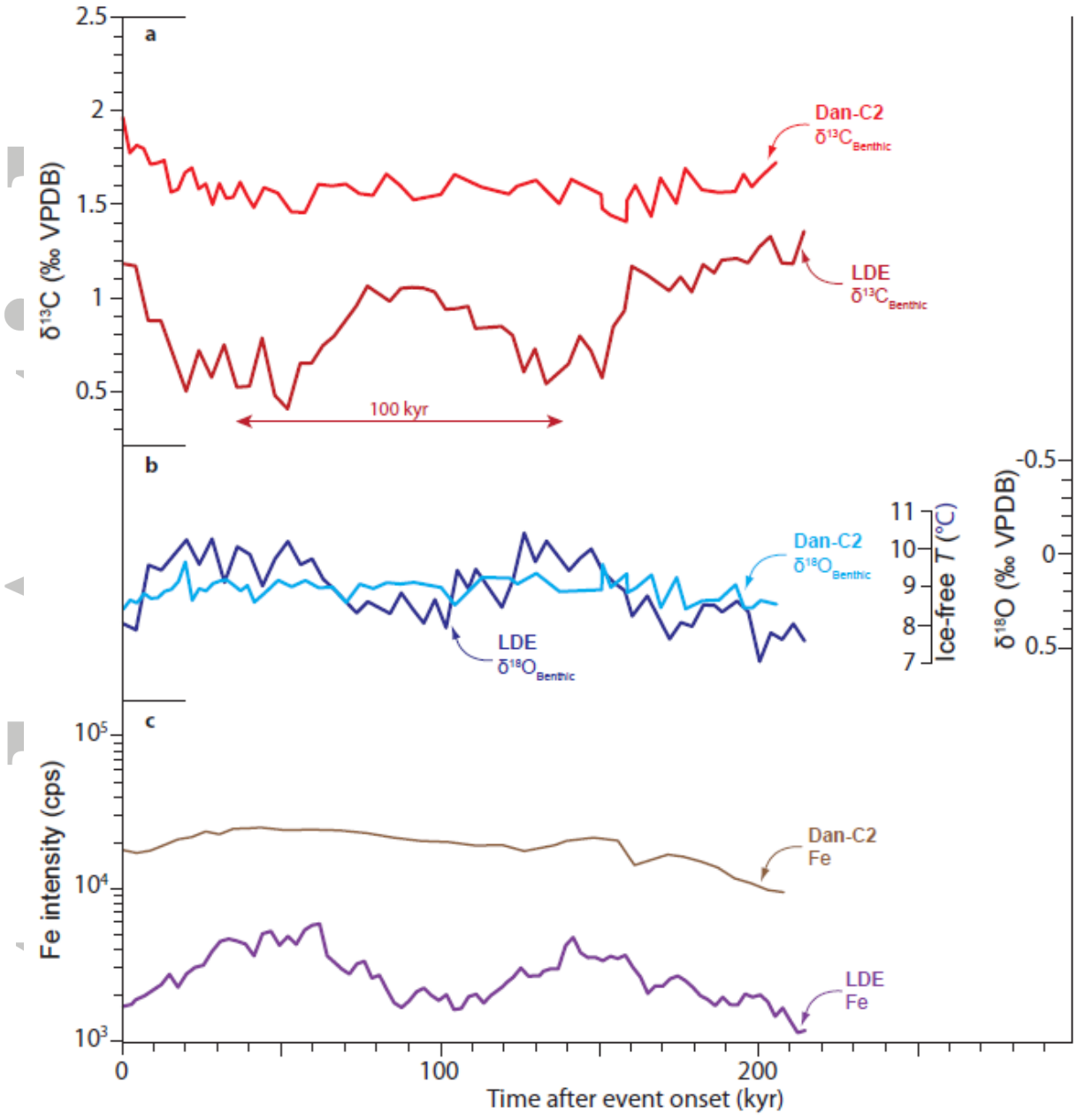


Figure 5. Comparison between the stable isotope and geochemical expressions of the Dan-C2 event and Latest Danian Event (LDE) at ODP Site 1262, plotted relative to time since onset of the respective events: (**a**) benthic stable carbon isotope ($\delta^{13}C_{benthic}$) records; (**b**) benthic stable oxygen isotope ($\delta^{18}O_{benthic}$) records; (**c**) Fe intensity records (Westerhold et al., 2008).

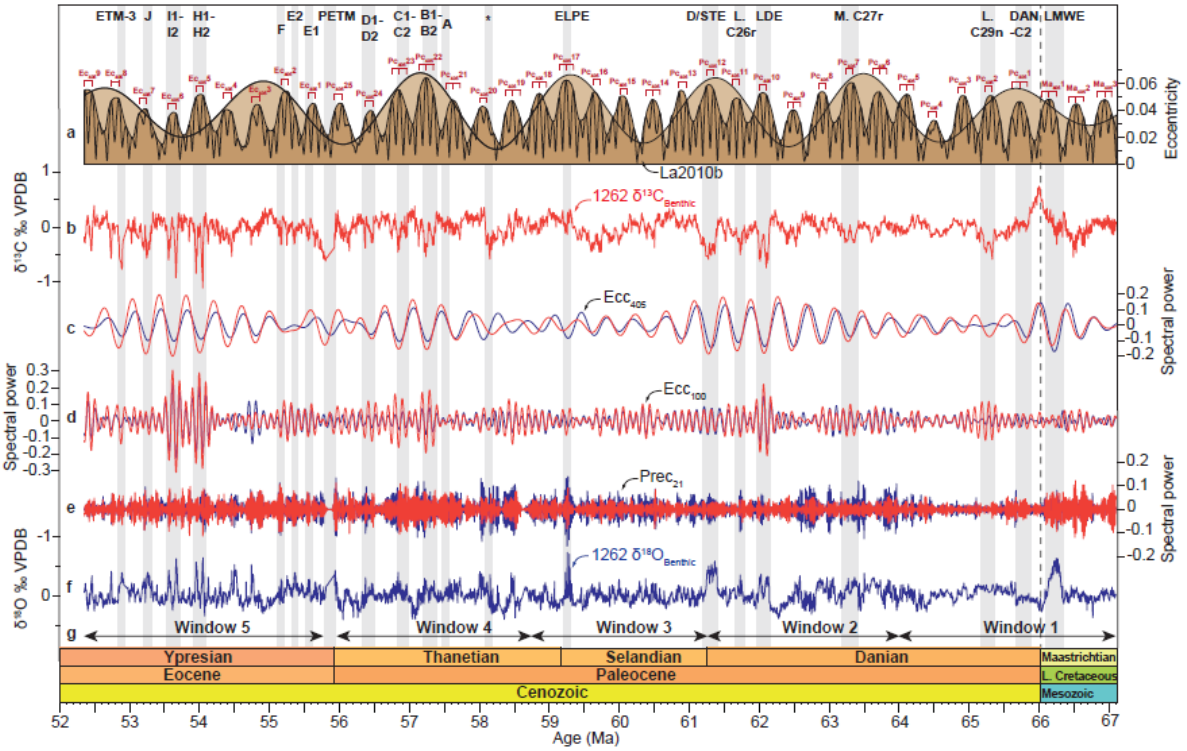


Figure 6. Gaussian filters at the principle Milankovitch frequencies for the benthic stable carbon isotope record ($\delta^{13}C_{benthic}$, red) and benthic stable oxygen isotope record ($\delta^{18}O_{benthic}$, blue) from ODP Site 1262. (**a**) La2010b orbital solution (Laskar et al., 2011), with long eccentricity (405-kyr) maxima illustrated in dark brown and the filtered ~2.4 million year modulation of eccentricity illustrated in pale brown. 405-kyr eccentricity maxima are labelled in red following the nomenclature of Husson et al. (2011) for the Maastrichtian, Dinarès-Turell et al. (2014) for the Paleocene, and Westerhold and Röhl (2009) for the Eocene. (**b**) Detrended $\delta^{13}C_{benthic}$ data. (**c**) Long eccentricity (405-kyr) filter. (**d**) Short eccentricity (100-kyr) filter. (**e**) Precession (21-kyr) filter. (**f**) Detrended $\delta^{18}O_{benthic}$ data. (**g**) Temporal distribution of discrete time windows used in Figure 8 and Figure 10.

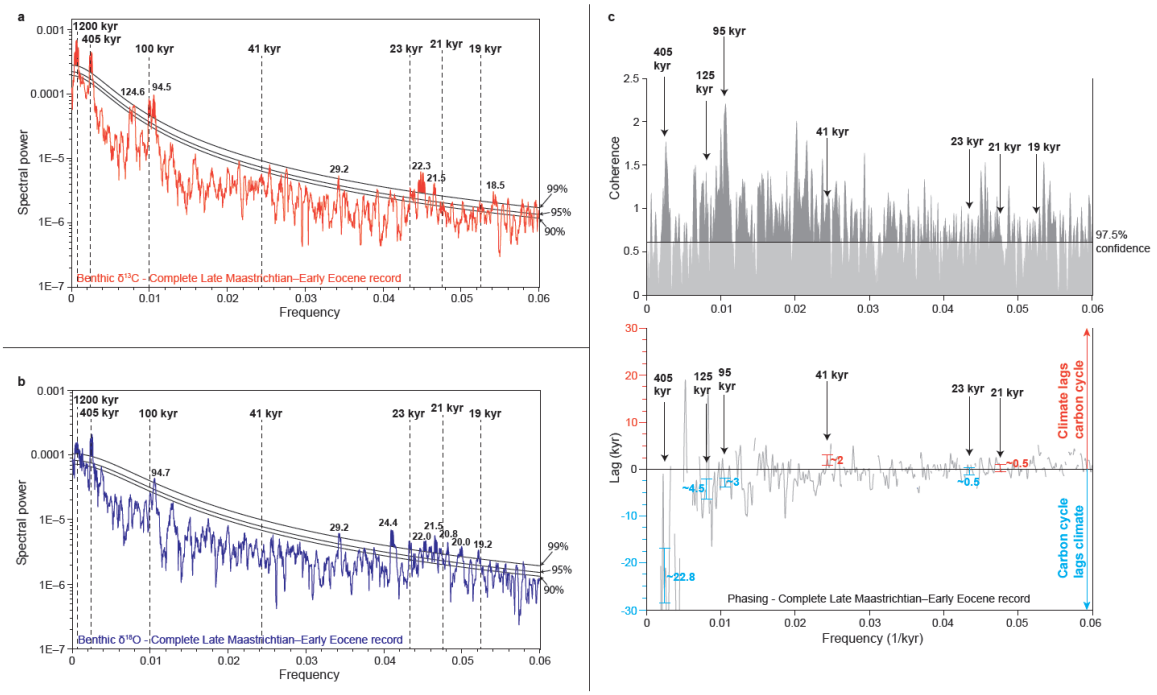


Figure 7. Multi-Taper Method (MTM) power spectra and phasing for the $\delta^{13}C_{benthic}$ and $\delta^{18}O_{benthic}$ records from ODP Site 1262. (**a**) MTM power spectra for the complete Late Maastrichtian–Early Eocene (67.10–52.35 Ma) $\delta^{13}C_{benthic}$ record. The resolution of our $\delta^{13}C_{benthic}$ record enables the split eccentricity peaks at ~125 and ~95 kyr to be resolved. (**b**) MTM power spectra for the complete Late Maastrichtian–Early Eocene (67.10–52.35 Ma) $\delta^{18}O_{benthic}$ record. (**c**) Average coherence and phasing between the ODP Site 1262 $\delta^{13}C_{benthic}$ and $\delta^{18}O_{benthic}$ records spanning the Late Maastrichtian–Early Eocene (67.10–52.35 Ma). On the coherence spectra, frequencies above the 97.5% confidence level are considered coherent, for which the phasing between $\delta^{13}C_{benthic}$ and $\delta^{18}O_{benthic}$ was calculated. Negative values for the phasing (lag) in blue indicate that $\delta^{13}C_{benthic}$ lags $\delta^{18}O_{benthic}$ (i.e., carbon cycle lags climate), whilst positive values in red indicate $\delta^{18}O_{benthic}$ lags $\delta^{13}C_{benthic}$ (i.e., climate lags carbon cycle). Values for the mean lag (in kyr) are indicated, with error at the 97.5% confidence level indicated by vertical bars.

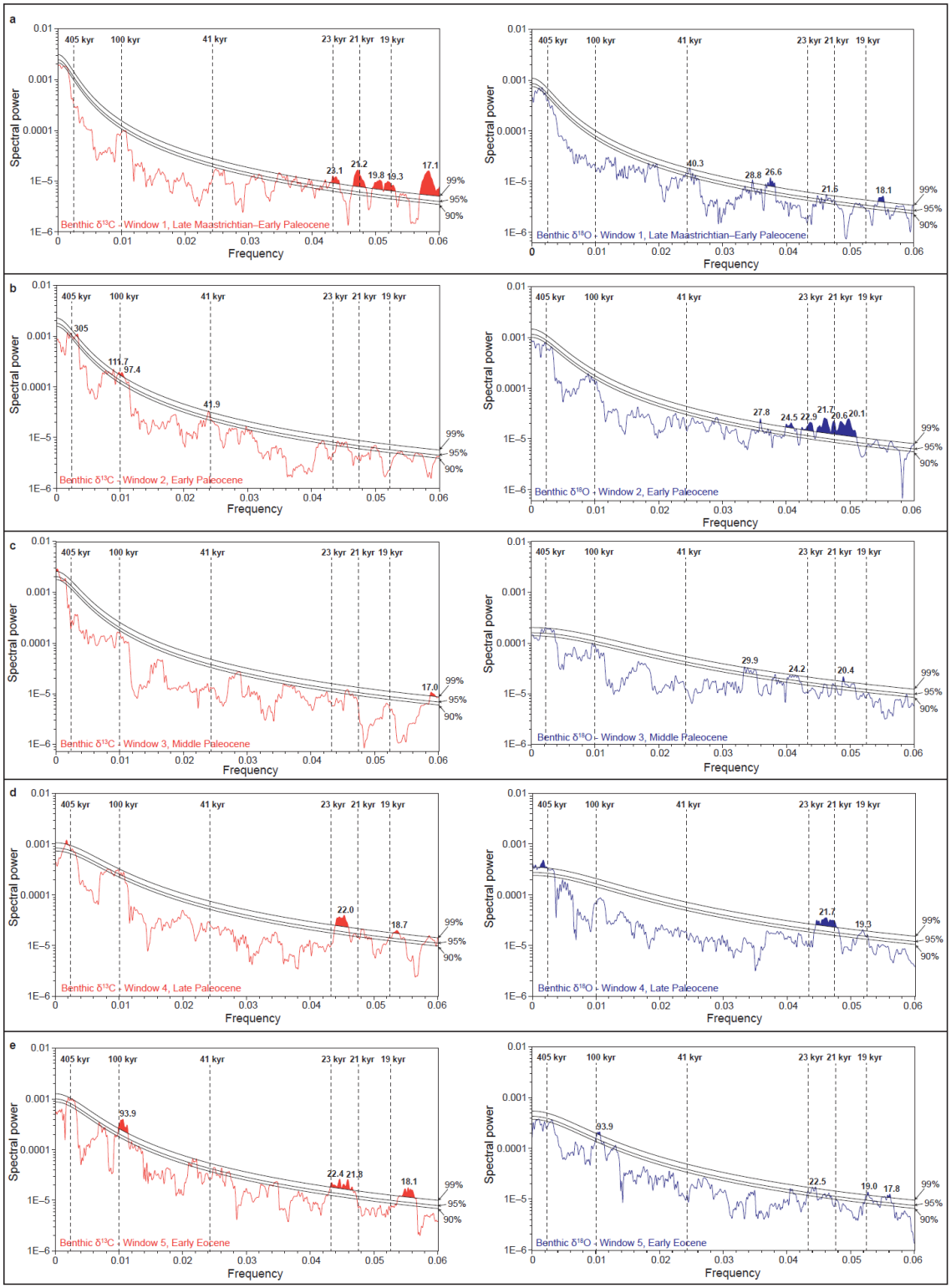


Figure 8. Multi-Taper Method (MTM) power spectra for the $\delta^{13}C_{benthic}$ record (in red) and $\delta^{18}O_{benthic}$ record (in blue) for the 5 discrete time windows. (**a**) Window 1, Late Maastrichtian–Early Paleocene (67.1–64.0 Ma). (**b**) Window 2, Early Paleocene (64.0–61.25 Ma). (**c**) Window 3, Middle Paleocene (61.25–58.75 Ma). (**d**) Window 4, Late Paleocene (58.75–55.93 Ma). (**e**) Window 5, Early Eocene (55.83–52.35 Ma). Temporal distribution of the time windows is illustrated in Figure 2f and Figure 6g.

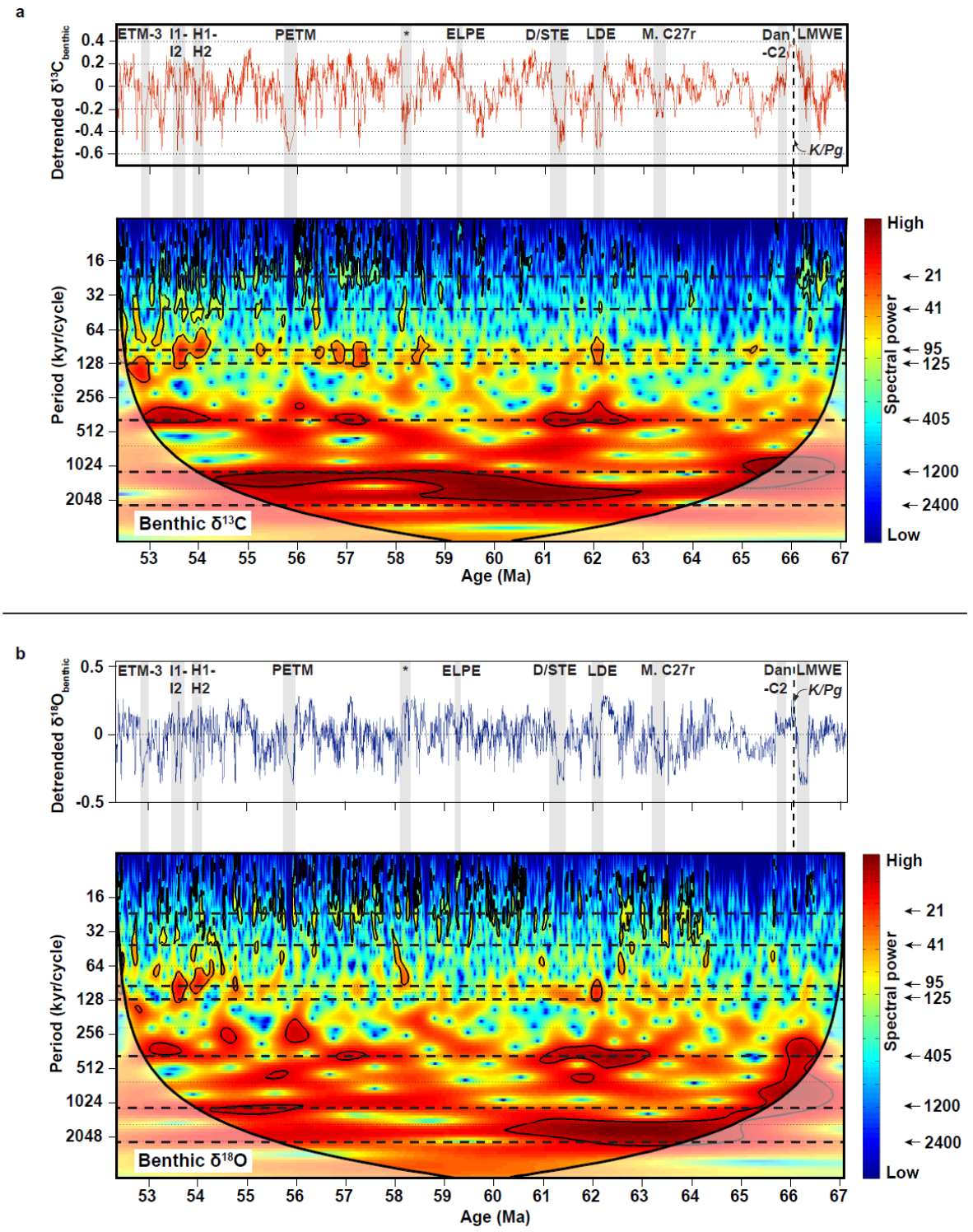


Figure 9. Evolutionary wavelet spectra for the complete Late Maastrichtian–Early Eocene records from ODP Site 1262. Milankovitch cycles (in kyr) are indicated by dashed lines across the spectra and labelled with arrows along the right-hand margin. (**a**) $\delta^{13}C_{benthic}$. (**b**) $\delta^{18}O_{benthic}$.

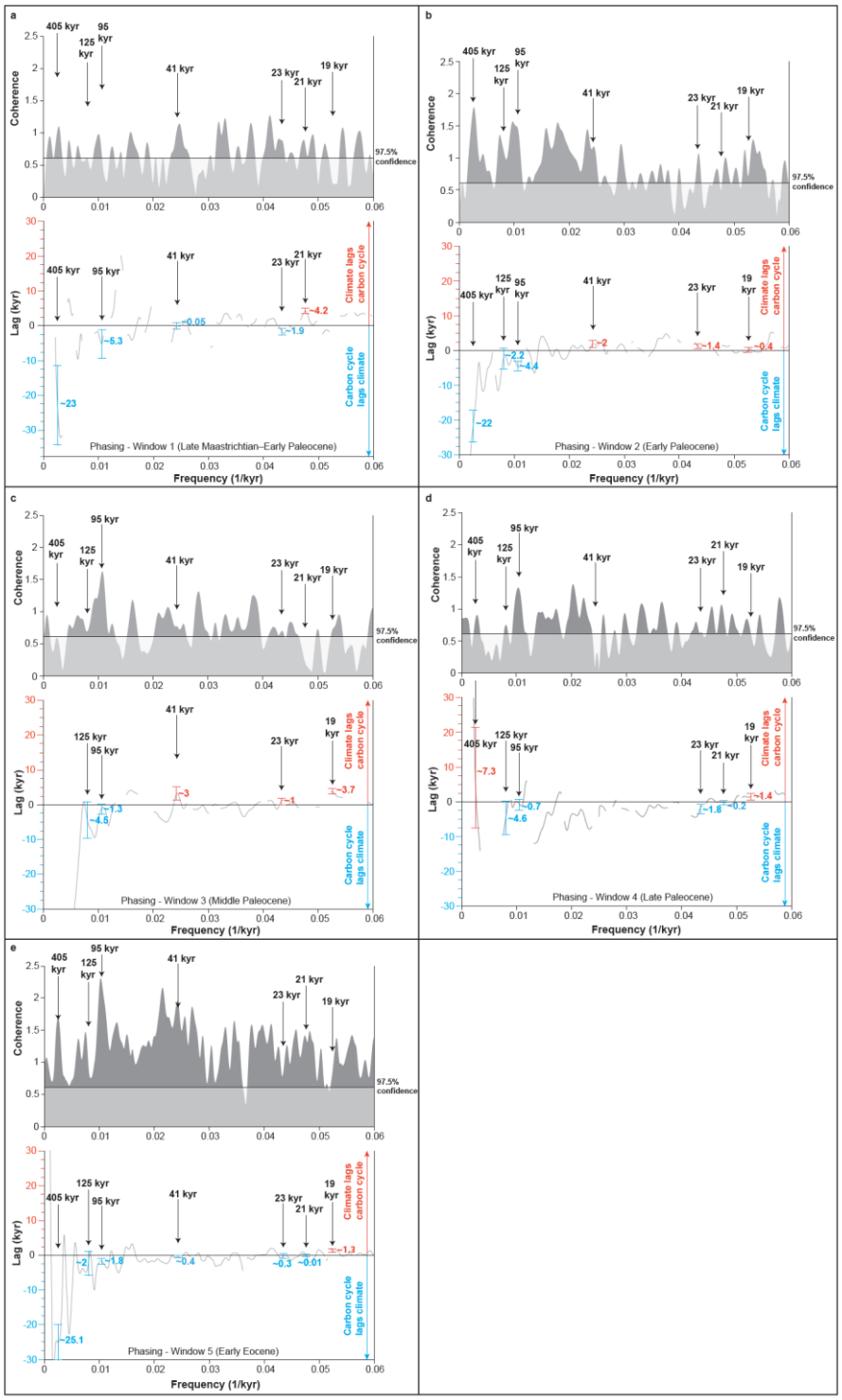


Figure 10. Coherence and phasing between the $\delta^{13}C_{benthic}$ and $\delta^{18}O_{benthic}$ records for the 5 discrete time windows. On the coherence spectra, frequencies above the 97.5% confidence level are considered coherent, for which the phasing between $\delta^{13}C_{benthic}$ and $\delta^{18}O_{benthic}$ was calculated. Negative values for the phasing (lag) in blue indicate that $\delta^{13}C_{benthic}$ lags $\delta^{18}O_{benthic}$ i.e., carbon cycle lags climate, whilst positive values in red indicate $\delta^{18}O_{benthic}$ lags $\delta^{13}C_{benthic}$ i.e., climate lags carbon cycle. Values for the mean lag (in kyr) are indicated, with the range of values indicated by error bars. (**a**) Window 1, Late Maastrichtian–Early Paleocene (67.1–64.0 Ma). (**b**) Window 2, Early Paleocene (64.0–61.25 Ma). (**c**) Window 3, Middle Paleocene (61.25–58.75 Ma). (**d**) Window 4, Late Paleocene (58.75–55.93 Ma). (**e**) Window 5, Early Eocene (55.83–52.35 Ma). Temporal distribution of the time windows is illustrated in Figure 2f and Figure 6g.